

Majorana bound states in a superconducting Rashba nanowire deposited on an antiferromagnetic surface

Aksel Kobińska,^{1,*} Nicholas Sedlmayr,^{1,†} and Andrzej Ptok^{2,‡}

¹*Institute of Physics, Maria Curie-Skłodowska University,
Plac Marii Skłodowskiej-Curie 1, PL-20031 Lublin, Poland*

²*Institute of Nuclear Physics, Polish Academy of Sciences,
ul. W. E. Radzikowskiego 152, PL-31342 Kraków, Poland*

(Dated: March 2, 2022)

Theoretical studies have shown that Majorana bound states can be induced at the ends of a one dimensional wire, a phenomenon possible due to the interplay between s-wave superconductivity, spin-orbit coupling, and an external magnetic field. These states have been observed in superconductor–semiconductor hybrid nanostructures in the presence of a Zeeman field, and in the limit of a low density of particles. In this paper, we demonstrate and discuss the possibility of the emergence of Majorana bound states in a superconducting Rashba nanowire deposited on an antiferromagnetically ordered surface. We calculate the relevant topological invariant in several complementary ways. Studying the topological phase diagram reveals two branches of the non-trivial topological phase—a main branch, which is typical for Rashba nanowires, and an additional branch emerging due to the antiferromagnetic order. In the case of the additional topological branch, Majorana bound states can also exist close to half-filling, obviating the need for either doping or gating the nanowire to reach the low density regime. Moreover, we show the emergence of the Majorana bound states in the absence of the external magnetic field, which is possible due to the antiferromagnetic order. We also discuss the properties of the bound states in the context of real space localization and the spectral function of the system. This allows one to perceive the band inversion within the spin and sublattice subspaces in the additional branch, contrary to the main branch where the only band inversion reported in previous studies exists in the spin subspace. Finally we demonstrate how these topological phases can be confirmed experimentally in transport measurements.

I. INTRODUCTION

The possibility for topologically protected localized zero energy states to form in a superconducting nanowire was first proposed in a seminal paper by Kitaev [1], and opened a period of intense study of these Majorana bound states (MBS) [2–4]. The states are of particular interest because they are non-Abelian anyons, and thus potentially of interest for topological quantum computing [5]. In the last decade, potential signatures of MBS have been detected in low-dimensional structures, e.g. semiconducting–superconducting hybrid nanostructures [6–13] and chains of magnetic atoms deposited on a superconducting surface [14–19]. In the first case it is the interplay between intrinsic spin–orbit coupling (SOC), proximity induced superconductivity, and an external magnetic field, which leads to the emergence of MBS [3]. In the second case, MBS are expected due to the helical ordering of magnetic moments in the mono-atomic chains [20–25].

MBS emerge in these systems when they are in a topologically non-trivial phase. In a typical situation, the phase transition from topologically trivial to non-trivial is induced by the magnetic field [26–28]. Increasing the

applied magnetic field leads to a closing of the trivial superconducting gap and the reopening of a new, non-trivial, gap [29]. This is true for a system with a relatively small density of particles, i.e. when the Fermi level is near the bottom of the band. If the splitting of the bands by the external magnetic field is larger than the superconducting gap, pairing occurs in the one-band channel [8, 29–31]. This “one” type quasiparticle pairing arises as an effect of the spin mixing by the SOC, corresponding to *p*-wave inter-site pairing in real space [32–34].

However, state of the art experiments also allow one to create inhomogeneous periodic magnetic fields. For example, carbon nanotubes coupled to an antiferromagnetic substrate [35] lead to a *synthetic magnetic field* [36]. Similar solutions were proposed theoretically in the form of nanomagnets [37–39], which have also been executed experimentally with an arrangement of alternating magnetization [40–42]. Just like in the case of the magnetic moments with helical order [20–23], this magnetic field can be the source of an effective spin–orbit coupling. Another possibility consists of magnetic nanopillars producing magnetic textures, which can be tuned by passing currents [43]. Similar types of architecture based on magnetic tunnel junctions can be used to perform braiding operations [44]. Last, but not least, coupling a nanowire to a magnetic Co/Pt-multilayer [45] can achieve a similar goal.

New perspectives for a system with antiferromagnetic (AFM) order were brought about by recent progress in experimental techniques allowing for the preparation of

* e-mail: akob@kft.umcs.lublin.pl

† e-mail: sedlmayr@umcs.pl

‡ e-mail: aptok@mmj.pl

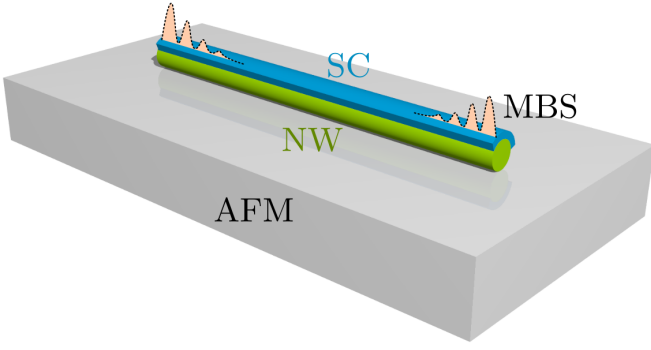


Figure 1. Schematic representation of the described system – semiconducting nanowire (NW) deposited on the surface of an antiferromagnetic (AFM) base, partially covered by a superconductor (SC). At the end of the nanowire, Majorana bound states (MBS) can be induced due to the interplay between intrinsic spin orbit coupling, external Zeeman magnetic field (along the nanowire), superconductivity and antiferromagnetism (induced by the proximity effect).

atomic chains [19]. In such a case a self-organized spin helix order [20–22] can be stabilized via the Ruderman–Kittel–Kasuya–Yosida (RKKY) mechanism [46–48]. The AFM order was observed experimentally in sufficiently short Fe chains [49, 50]. Moreover, the proximity effect can relay the AFM order to the nanowire, e.g. by contact with a strong AFM system (cf. Fig. 1). Strong antiferromagnets such as YbCo₂Si₂ [51], VBr₃ [52], Mn₂C [53], NiPS₃ [54], or most promisingly V₅S₈ [55, 56], can be good candidates for the substrate in the investigated system. In such a case, tuning of the topological phase can emerge due the external magnetic field without destroying the AFM order in the substrate.

In the case of a semiconducting–superconducting hybrid nanowire, the non-trivial topological phase is expected when the Fermi level is located near the bottom of the band. Otherwise too large a magnetic field is required. As a result, the MBS is strongly restricted to the case of a low density of particles in the system. Contrary to this, we discuss a scenario for MBS in the nearly-half-filled case. Moreover, contrary to most previous studies, we show the presence of MBS without any *additional* external magnetic field applied [57, 58], but instead only due to the AFM order.

This paper is organized as follows. In Sec. II, we describe our model and the techniques used to investigate it. In Sec. III, we derive the topological phase diagram of the system in the presence of AFM order and external magnetic field. We also discuss the origin of the non-trivial topological phase. In Sec. IV, we discuss electronic properties of the system in both real and reciprocal spaces. Next, in Sec. V, we discuss the proposal of an experimental examination of this phase diagram via the differential conductance. Finally, in Sec. VI, we summarize the results.

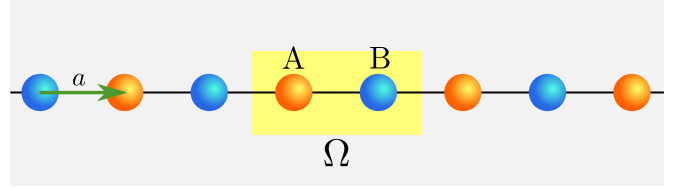


Figure 2. The one dimensional AFM lattice discussed in this paper. The unit cell Ω contains two non-equivalent sites with opposite magnetic moments (orange and blue) belonging to sublattices A and B. The lattice spacing $a \equiv 1$ is taken as the distance between two nearest-neighbor sites.

II. MODEL AND TECHNIQUES

A. Real space description

In our calculations, we model the system shown schematically in Fig. 2. We consider a one dimensional Rashba nanowire with superconducting and antiferromagnetic order both induced by proximity effects (cf. Fig. 1), in the presence of an external magnetic field directed along the nanowire. The low energy physics of such a system can be described by the Hamiltonian $\mathcal{H} = \mathcal{H}_0 + \mathcal{H}_{\text{SC}} + \mathcal{H}_{\text{AFM}}$.

The Rashba nanowire itself is described by

$$\mathcal{H}_0 = \sum_{ij,ss',\sigma} \left[-t_{ij}^{ss'} - (\mu + \sigma h) \delta_{ij} \delta_{ss'} \right] c_{is\sigma}^\dagger c_{js'\sigma} \quad (1)$$

$$- i\lambda \sum_{i,\sigma\sigma'} \left[c_{iA\sigma}^\dagger \sigma_{\sigma\sigma'}^y c_{iB\sigma'} + c_{iB\sigma}^\dagger \sigma_{\sigma\sigma'}^y c_{i+1,A\sigma'} \right] + \text{H.c.},$$

where $c_{is\sigma}^\dagger$ ($c_{is\sigma}$) describes the creation (annihilation) of an electron with spin $\sigma \in \{\uparrow, \downarrow\}$ in sublattice $s \in \{A, B\}$ of the i -th unit cell. We assume equal hopping between the nearest-neighbor sites (when $t_{ij}^{ss'} = t = 1$ in appropriate energy units) and zero otherwise. As usual, μ is the chemical potential, and h is the external Zeeman magnetic field. In our calculations we neglect the orbital effect [59], assuming the magnetic field is parallel to the nanowire. The term in the second line describes the SOC with strength λ , where σ_y is the second Pauli matrix. Superconductivity, which is induced in a nanowire due to the proximity effect, can be described by the BCS-like term:

$$\mathcal{H}_{\text{SC}} = \Delta \sum_{is} \left(c_{is\uparrow}^\dagger c_{is\downarrow}^\dagger + c_{is\downarrow} c_{is\uparrow} \right), \quad (2)$$

where Δ is the superconducting order parameter (SOP), proportional to the induced superconducting gap. The AFM order in the nanowire is described by

$$\mathcal{H}_{\text{AFM}} = -m_0 \sum_{i\sigma} \sigma \left(c_{iA\sigma}^\dagger c_{iA\sigma} - c_{iB\sigma}^\dagger c_{iB\sigma} \right) \quad (3)$$

where m_0 denotes the amplitude of the AFM order.

Finite size system. — Properties of the finite size system (with open boundary conditions), can be analyzed in real space. In this case, the Hamiltonian \mathcal{H} can be diagonalized by the transformation $c_{is\sigma} = \sum_n (u_{isn\sigma}\gamma_n - \sigma v_{isn\sigma}^*\gamma_n^\dagger)$ [60], where γ_n and γ_n^\dagger are fermionic operators. Such a transformation leads to the real space Bogoliubov–de Gennes (BdG) equations [61], in the form $\mathcal{E}_n \Psi_{isn} = \mathbb{H}_{is,j's'} \Psi_{js'n}$, where $\mathbb{H}_{is,j's'}$ is the Hamiltonian in the matrix form, given in Appendix A.

From solving the BdG equations, we can determine the site-dependent average number of particles:

$$\begin{aligned} n_{is\sigma} &= \langle c_{is\sigma}^\dagger c_{is\sigma} \rangle \\ &= \sum_n [|u_{isn\sigma}|^2 f(\mathcal{E}_n) + |v_{isn\sigma}|^2 f(-\mathcal{E}_n)], \end{aligned} \quad (4)$$

where $f(\omega) = 1/[1 + \exp(-\omega/k_B T)]$ is the Fermi–Dirac distribution. From this, *effective* site-dependent magnetization is given as $m_{is} = n_{is\uparrow} - n_{is\downarrow}$. In similar way, we can determine the local density of states (LDOS) [62]:

$$\begin{aligned} \rho_{is}(\omega) &= -\frac{1}{\pi} \sum_{\sigma} \text{Im} G_{is\sigma}(\omega + i0^+) \\ &= \sum_{n\sigma} [|u_{isn\sigma}|^2 \delta(\omega + \mathcal{E}_n) + |v_{isn\sigma}|^2 \delta(\omega - \mathcal{E}_n)], \end{aligned} \quad (5)$$

where $G_{is\sigma} = \langle c_{is\sigma} | (\omega - H)^{-1} | c_{is\sigma}^\dagger \rangle$ and $\delta(\omega)$ is the Dirac delta function. The LDOS represents quantities experimentally measured by scanning tunneling microscope (STM) [63–66], and can give information about the emergence of the zero-energy states [14]. In the numerical calculations, we replace the delta function by the Lorentzian $\delta(\omega) = \xi/[\pi(\omega^2 + \xi^2)]$, with a small broadening $\xi/t = 0.001$.

B. Reciprocal space description

From the explicit form the Fourier transform of operators:

$$c_{is\sigma}^\dagger = \frac{1}{\sqrt{N}} \sum_{\mathbf{k}} c_{\mathbf{k}s\sigma}^\dagger \exp(-i\mathbf{k} \cdot \mathbf{R}_{is}), \quad (6)$$

where \mathbf{R}_{is} denotes position of i -th sites in sublattice s (cf. Fig. 2), the Hamiltonian in momentum space can be found:

$$\begin{aligned} \mathcal{H}_0 &= \sum_{\mathbf{k}\sigma} \mathcal{E}_{\mathbf{k}} \left(c_{\mathbf{k}A\sigma}^\dagger c_{\mathbf{k}B\sigma} + \text{H.c.} \right) \\ &\quad - \sum_{\mathbf{k}s\sigma} (\mu - \sigma h) c_{\mathbf{k}s\sigma}^\dagger c_{\mathbf{k}s\sigma} \\ &\quad + \sum_{\mathbf{k}\sigma\sigma'} i\mathcal{L}_{\mathbf{k}} \left(c_{\mathbf{k}A\sigma}^\dagger \sigma_{\sigma\sigma'}^y c_{\mathbf{k}B\sigma'} + \text{H.c.} \right), \end{aligned} \quad (7)$$

$$\mathcal{H}_{\text{SC}} = \Delta \sum_{\mathbf{k}s} \left(c_{\mathbf{k}s\uparrow}^\dagger c_{-\mathbf{k}s\downarrow}^\dagger + c_{-\mathbf{k}s\downarrow} c_{\mathbf{k}s\uparrow} \right), \quad (8)$$

$$\mathcal{H}_{\text{AFM}} = -m_0 \sum_{\mathbf{k}s\sigma} \sigma \left(c_{\mathbf{k}A\sigma}^\dagger c_{\mathbf{k}A\sigma} - c_{\mathbf{k}B\sigma}^\dagger c_{\mathbf{k}B\sigma} \right), \quad (9)$$

where $c_{\mathbf{k}s\sigma}^\dagger$ ($c_{\mathbf{k}s\sigma}$) describes the creation (annihilation) operator of an electron with momentum \mathbf{k} and spin σ in sublattice s . Additionally, $\mathcal{E}_{\mathbf{k}} = -2t \cos(k)$ denotes the dispersion relation of non-interacting electrons in a 1D chain, while $\mathcal{L}_{\mathbf{k}} = -2i\lambda \sin(k)$ is SOC in momentum space.

For the following we will use a more convenient representation for the Hamiltonian. We introduce Pauli matrices that act in the particle-hole subspace $\boldsymbol{\tau}^{0,x,y,z}$, spin subspace $\boldsymbol{\sigma}^{0,x,y,z}$, and sublattice subspace $\boldsymbol{\rho}^{0,x,y,z}$. The “0” superscript labels the identity matrix for any given subspace. Then, following the Bogoliubov transform, the Hamiltonian in the Nambu basis,

$$\begin{aligned} \psi_{\mathbf{k}}^\dagger &= \\ &\left(c_{\mathbf{k}A\uparrow}^\dagger c_{\mathbf{k}B\uparrow}^\dagger c_{\mathbf{k}A\downarrow}^\dagger c_{\mathbf{k}B\downarrow}^\dagger c_{-\mathbf{k}A\uparrow} c_{-\mathbf{k}B\uparrow} c_{-\mathbf{k}A\downarrow} c_{-\mathbf{k}B\downarrow} \right), \end{aligned} \quad (10)$$

takes the form $\mathcal{H} = \sum_{\mathbf{k}} \psi_{\mathbf{k}}^\dagger \mathcal{H}(\mathbf{k}) \psi_{\mathbf{k}}$, where

$$\begin{aligned} \mathcal{H}(\mathbf{k}) &= \mathcal{E}_{\mathbf{k}} \boldsymbol{\tau}^z \boldsymbol{\sigma}^0 \boldsymbol{\rho}^x - \mu \boldsymbol{\tau}^z \boldsymbol{\sigma}^0 \boldsymbol{\rho}^0 + i\mathcal{L}_{\mathbf{k}} \boldsymbol{\tau}^z \boldsymbol{\sigma}^y \boldsymbol{\rho}^x \\ &\quad - \Delta \boldsymbol{\tau}^y \boldsymbol{\sigma}^y \boldsymbol{\rho}^0 - h \boldsymbol{\tau}^z \boldsymbol{\sigma}^z \boldsymbol{\rho}^0 - m_0 \boldsymbol{\tau}^z \boldsymbol{\sigma}^z \boldsymbol{\rho}^z. \end{aligned} \quad (11)$$

We will use this form of the Hamiltonian to calculate the bulk topological properties. In turn, due to the bulk–boundary correspondence [67, 68], this tells us when there will be MBS in the finite length nanowire. More details can be found in Sec. III.

Band structure. — The band structure of the system can be found by diagonalizing the Hamiltonian (11). Each block $\mathcal{H}_{\mathbf{k}}$ has eight eigenvalues $\mathcal{E}_{\mathbf{k}}^n$ (for $n = 1, 2, \dots, 8$) associated with eigenvectors

$$\begin{aligned} \varphi_{\mathbf{k}} &= \\ &\left(u_{\mathbf{k}A\uparrow}^n u_{\mathbf{k}B\uparrow}^n u_{\mathbf{k}A\downarrow}^n u_{\mathbf{k}B\downarrow}^n v_{\mathbf{k}A\uparrow}^n v_{\mathbf{k}B\uparrow}^n v_{\mathbf{k}A\downarrow}^n v_{\mathbf{k}B\downarrow}^n \right)^T. \end{aligned} \quad (12)$$

Due to the existence of the AFM order in the system, the unit cell Ω contains two non-equivalent sites. Increasing the size of the unit cell twice leads to the folding of the Brillouin zone (BZ) to $\mathbf{k} \in [-\pi/2, \pi/2]$. As a result the two time-reversal invariant momenta (TRIM) [69, 70] are $\mathbf{k} = 0$ and $\mathbf{k} = \pi/2$.

Let us briefly discuss the influence of the separate Hamiltonian terms on the form of the band structure of the system without superconductivity (Fig. 3). In the case of a “free standing” chain (i.e. in the absence of magnetic field, AFM order, and SOC), the bands contain two spin degenerate branches due to the unit cell containing two, in this case identical, atoms [dashed line in panel (a)]. These two branches are a result of the folding of the $\mathcal{E}_{\mathbf{k}} = -2t \cos(k_x a)$ dispersion relation, intersecting at $\mathbf{k} = \pm\pi/2$. The introduction of AFM order into the system allows for a band gap to emerge at $\mathbf{k} = \pi/2$ [indicated by the red marker at panel (a)]. Such a band gap exist in the band structure independently of μ and the other parameters. Here, the spin degree of freedom

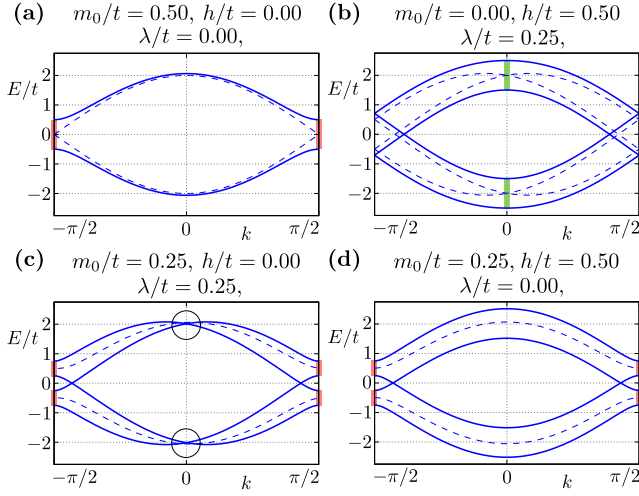


Figure 3. The impact of the model parameters on the band structure of the chain without superconductivity ($\Delta = 0$). (a) The AFM order leads to the opening of the band gap at $k = \pm\pi/2$. Here, the dashed lines show bands in the absence of the AFM order. (b) The spin-orbit coupling leads to a shifting of bands in the momentum domain (dashed line), while the magnetic field lifts the degeneracy at $k = 0$. (c) In the presence of the AFM order, the spin-orbit coupling leads to a shifting of the bands in the momentum domain, while preserving the band degeneracy at $k = 0$ (indicated by circles). (d) The external magnetic field leads to a shifting of the bands in the energy domain due to the Zeeman effect. In panels (c) and (d), the dashed line shows bands from panel (a). Green (red) markers at $k = 0$ ($k = \pm\pi/2$) indicate points with lifted degeneracy by the magnetic field (AFM order). Results obtained for several fixed parameters (as labeled) and a chemical potential $\mu/t = 0$.

remains a good quantum number, but not the sublattice degree of freedom [71]. This yields a situation where eigenstates are a spin-dependent mixture of the A and B sublattice states. Moreover, the spatial profile displays a lattice dependent modulation of the density that is spin dependent and band dependent. Breaking time reversal symmetry due to AFM order still provides an analogue to Kramers' theorem due to the combined time reversal and translation symmetry — hence there are two degenerate bands with opposite spins. As a result, this degeneracy can be lifted by an external magnetic field (or SOC).

This can be seen on panel (b), where Rashba type SOC shifts the bands along the k axis in opposite directions [dashed lines]. Here, it should be mentioned that this effect is typical in the Rashba chain [72, 73]. Introducing the Zeeman magnetic field h removes the band degeneracy by breaking time reversal symmetry, resulting in an energy shift. In the presence of the SOC [solid line at panel (b)], the magnetic field lifts the degeneracy at $k = 0$ [indicated by the green markers at panel (b)].

A similar effect of the spin-orbit coupling is observed in the presence of the AFM order [panel (c)], where we observe band shifting along the k axis, while the band gap

changes along the E axis (solid lines). Here, dashed lines show bands in the presence only of AFM order [i.e. the solid lines from panel (a)]. At the same time, the degeneracy at $k = 0$ (indicated by circles) is preserved. A very strong magnetic field can lift this degeneracy (not shown).

Finally, the external magnetic field in the presence of the AFM order [panel (d)] lifts the spin-degeneracy [observed at (a)] while simultaneously preserving the band gap at $k = \pm\pi/2$. As the AFM order introduces a band splitting at lower energies than in the standard scenario, we may expect that we can drive the chain into the non-trivial phase at densities closer to the half-filling case. As we shall see in the following, this is indeed the case.

III. TOPOLOGICAL PHASE DIAGRAM

In this section, we will discuss the topological phase diagrams obtained from analytical calculations of the invariants and numerical calculations. We will also consider them in the context of the localization of the Majorana zero modes at the ends of the system. Based on the symmetries of the system, we will discuss the origin of the topological phase and the impact of the AFM order.

A. System symmetries

The BdG Hamiltonian (11) can possess several symmetries important for its topological properties [74, 75]. Of interest are anti-unitary symmetries and we have:

- (i) The particle-hole (PH) symmetry described by the anti-unitary operator $\mathcal{P} = \tau^x \sigma^0 \rho^0 \mathcal{K}$, such that $\mathcal{P} H_{\mathbf{k}} \mathcal{P}^{-1} = -H_{-\mathbf{k}}$ and $\mathcal{P}^2 = 1$. \mathcal{K} is the complex conjugation operator. It is worth mentioning, that all BdG Hamiltonians satisfy PH symmetry by construction [75].
- (ii) The “time-reversal” (TR) symmetry described by the anti-unitary operator $\mathcal{T} = \Lambda \mathcal{K}$, where $\Lambda = \tau^0 \sigma^0 \rho^0$, and $\mathcal{T} H_{\mathbf{k}} \mathcal{T}^{-1} = H_{-\mathbf{k}}$ with $\mathcal{T}^2 = 1$. Note that this is not the physical time-reversal operator for the electrons.
- (iii) Finally we have the composite of these, the sublattice (SL) or “chiral” symmetry described by the unitary operator $\mathcal{S} = \mathcal{P} \mathcal{T} = \tau^x \sigma^0 \rho^0$, with $\mathcal{S}^{-1} H_{\mathbf{k}} \mathcal{S} = -H_{\mathbf{k}}$.

The impact of these symmetries on the Hamiltonian is schematically shown in the Fig. 4. With all of these symmetries present, which is the case for the Hamiltonian (11), we find ourselves in the BDI symmetry class in the Altland–Zirnbauer periodic-table of topological classes [75–77]. From this, the \mathbb{Z} invariant (i.e. the winding number w) can be studied in order to discuss the topological phase diagram. We can also construct a \mathbb{Z}_2

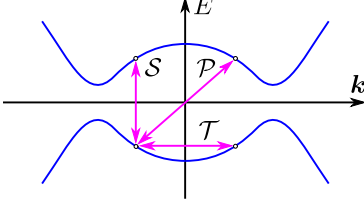


Figure 4. Schematic representation of the roles played by the symmetries possessed by the considered Hamiltonian. The particle-hole symmetry \mathcal{P} results in the symmetry of the spectrum (solid blue line) with respect of the point ‘zero’, while time-reversal symmetry \mathcal{T} and chiral (sublattice) symmetry \mathcal{S} correspond to reflection of the spectrum across the momentum and energy axes, respectively.

invariant (e.g. from the Pfaffian) which measures the parity of w . Both topological indices will be discussed below.

B. Topological invariants and origin of the topological phase

First we note that a Chiral Hamiltonian (11) can be rewritten in purely off-diagonal form [78] using the rotation $\tilde{\mathcal{H}}(\mathbf{k}) = \mathcal{U}_\pi^\dagger \mathcal{H}(\mathbf{k}) \mathcal{U}_\pi$ where $\mathcal{U}_\pi = e^{i\frac{\pi}{4}\tau^y} \sigma^0 \rho^0$. This results in

$$\tilde{\mathcal{H}}(\mathbf{k}) = \mathcal{E}_k \tau^x \sigma^0 \rho^x - \mu \tau^x \sigma^0 \rho^0 + i \mathcal{L}_k \tau^x \sigma^y \rho^x - \Delta \tau^y \sigma^y \rho^0 - h \tau^x \sigma^z \rho^0 - m_0 \tau^x \sigma^z \rho^z, \quad (13)$$

which has the form

$$\tilde{\mathcal{H}}(\mathbf{k}) = \begin{pmatrix} 0 & \mathcal{A}(\mathbf{k}) \\ \mathcal{A}^\dagger(-\mathbf{k}) & 0 \end{pmatrix}, \quad (14)$$

where

$$\mathcal{A}(\mathbf{k}) = \mathcal{E}_k \sigma^0 \rho^x - \mu \sigma^0 \rho^0 + i \mathcal{L}_k \sigma^y \rho^x + i \Delta \sigma^y \rho^0 - h \sigma^z \rho^0 - m_0 \sigma^z \rho^z. \quad (15)$$

The winding number w can be found starting from the standard chiral invariant [79]

$$w = \frac{1}{4\pi i} \int_{-\frac{\pi}{2}}^{\frac{\pi}{2}} dk \text{Tr} \mathcal{S} \tilde{\mathcal{H}} \partial_k \tilde{\mathcal{H}}^{-1}, \quad (16)$$

which has the equivalent formulation, found after a small amount of manipulation,

$$w = \frac{1}{2\pi i} \int_0^\pi dk \text{Tr} [\partial_k \mathcal{A}(k)] \mathcal{A}^{-1}(k). \quad (17)$$

This can be easily calculated numerically to find the chiral invariant. However in the following we will find an analytical formula for the invariant. Rewriting this as

$$w = \frac{1}{2\pi i} \int_0^\pi dk \partial_k \ln \det [\mathcal{A}(k)], \quad (18)$$

we see that the invariant is the winding of $\det \ln [\mathcal{A}(k)]$ across the Brillouin zone.

Now because

$$\det \mathcal{H}(\mathbf{k}) = \det \tilde{\mathcal{H}}(\mathbf{k}) = \det \mathcal{A}(\mathbf{k}) \cdot \det \mathcal{A}^\dagger(-\mathbf{k}), \quad (19)$$

the sign of the gap is encoded by the function $Z_{\mathbf{k}} = \det \mathcal{A}(\mathbf{k}) = \det \mathcal{A}^\dagger(-\mathbf{k})$, where from Eq. (15) we find

$$\begin{aligned} Z_{\mathbf{k}} = & (h_+^2 - \mu^2 - \Delta^2) (h_-^2 - \mu^2 - \Delta^2) \\ & + 8t^2 (2t^2 \cos^2(k) - h_- h_+ - \mu^2 + \Delta^2) \cos^2(k) \\ & + 8\lambda^2 (2\lambda^2 \sin^2(k) + h_- h_+ - \mu^2 + \Delta^2) \sin^2(k) \\ & - 16t^2 \lambda^2 \sin^2(k) \cos^2(k) + 32it \Delta \lambda \mu \cos(k) \sin(k), \end{aligned} \quad (20)$$

with $h_\pm = h \pm m_0$.

From the definition of $Z_{\mathbf{k}}$ and Eq. (18) one can see that the winding number of $z_{\mathbf{k}} = Z_{\mathbf{k}}/|Z_{\mathbf{k}}| = \exp(i\theta_{\mathbf{k}})$ is equivalently the invariant w and

$$w = \frac{-i}{2\pi} \int_{\mathbf{k}=-\pi/2}^{\mathbf{k}=\pi/2} \frac{dz_{\mathbf{k}}}{z_{\mathbf{k}}} = \frac{1}{2\pi} \int_{-\pi/2}^{\pi/2} d\mathbf{k} \frac{d\theta_{\mathbf{k}}}{d\mathbf{k}}. \quad (21)$$

This clearly takes only integer values (including zero) since $z_{-\pi/2} = z_{\pi/2}$. The winding number is associated with the number of times that the angle $\theta_{\mathbf{k}}$ winds about the origin in the complex plane (see Fig. 5). This quantity is invariant under smooth perturbation and cannot be changed unless $|Z_{\mathbf{k}}|$ goes to zero due to gap closing (provided the chiral symmetry is preserved). The winding number w is the \mathbb{Z} topological index.

As $\mathcal{A}(\mathbf{k})$ also has time reversal asymmetry $\mathcal{K} \mathcal{H}_k \mathcal{K} = \mathcal{H}_{-k}$, at the TRIM $\mathcal{A}(0, \pi/2)$ must be real, and hence so must $z_{0, \pi/2}$. Therefore for the topological index w to change one of $z_{0, \pi/2}$ must pass through zero, corresponding to a gap closing. The relative signs of $z_{0, \pi/2}$ therefore encode some information about the topological index, its parity $(-1)^w$. We can therefore construct a \mathbb{Z}_2 topological index [1]:

$$\mathcal{Q} = (-1)^w = \text{sgn}(z_{\mathbf{k}=0}) \cdot \text{sgn}(z_{\mathbf{k}=\pi/2}) \quad (22)$$

which is equivalent to the index based on the Pfaffian [1]

$$\mathcal{Q} = \text{sgn Pf} [\mathcal{W}(0)] \cdot \text{sgn Pf} [\mathcal{W}(\pi/2)], \quad (23)$$

where $\mathcal{W}(k) = \mathcal{H}(k) \Lambda$. Moreover, from the Hamiltonian (14) one finds:

$$\begin{aligned} \text{Pf} [\mathcal{W}(0)] = & (h_+^2 - \mu^2 - \Delta^2) (h_-^2 - \mu^2 - \Delta^2) \\ & + 8t^2 (2t^2 - h_- h_+ - \mu^2 + \Delta^2), \end{aligned} \quad (24)$$

and

$$\begin{aligned} \text{Pf} [\mathcal{W}(\pi/2)] = & (h_+^2 - \mu^2 - \Delta^2) (h_-^2 - \mu^2 - \Delta^2) \\ & + 8\lambda^2 (2\lambda^2 + h_- h_+ - \mu^2 + \Delta^2). \end{aligned} \quad (25)$$

Topological phase diagrams obtained from Eq. (22) are in agreement with those ones obtained from the winding number (Fig. 6), as well as from scattering matrix technique (Fig. 7, cf. Sec. III C).

As we have shown above, there exist a strong connection between \mathbb{Z} invariant w and the Pfaffian \mathbb{Z}_2 invariant [78]. As for this model $w \in \{-1, 0, 1\}$ then $\mathcal{Q} = 1$ refers to a topologically trivial phase and $\mathcal{Q} = -1$ refers to a topologically non-trivial phase. It is then straightforward to find the exact relation between both invariants for our model:

$$w = \frac{\text{sgn}(\Delta\lambda\mu)}{2} \{ \text{sgn Pf}[\mathcal{W}(\pi/2)] - \text{sgn Pf}[\mathcal{W}(0)] \}, \quad (26)$$

which follows from Eq. (20) and Eq. (18). Topological phase diagrams obtained from the winding number calculations are shown in Fig. 6.

Changes in \mathcal{Q} are related to changes in the sign of $\text{Pf}[\mathcal{W}(\mathbf{k})]$ at TRIM. In the absence of the AFM order ($h_{\pm} \rightarrow h$), only $\text{Pf}[\mathcal{W}(0)]$ changes sign with changes in h . This is shown as the typical form of the parabolic-like part on phase diagram [Fig. 6(a)]. However, the existence of the AFM order alone can also force the emergence of an additional branch in the topologically non-trivial phase. This is possible due to the sign change of $\text{Pf}[\mathcal{W}(\pi/2)]$

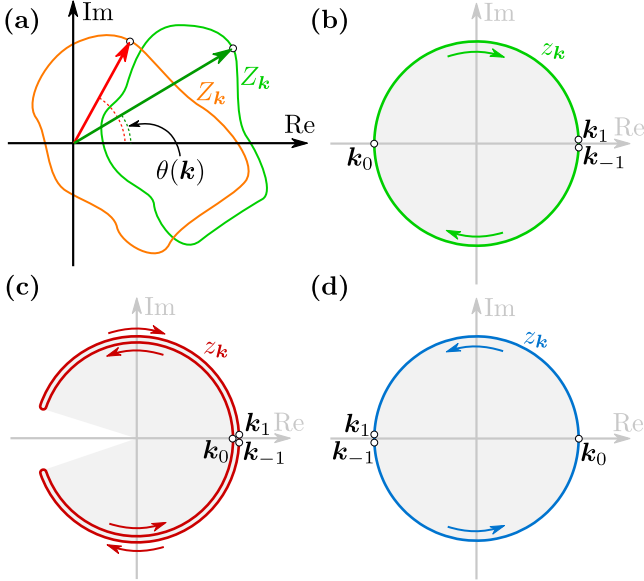


Figure 5. (a) Graphical interpretation of the winding number w , given by Eq. (21). $z_k = Z_k/|Z_k|$ corresponds to a projection of some closed contour given by Z_k on the unit circle. In the case of the non-trivial topological phase, the contour created by Z_k lies on the complex plane and contains the origin. Then, periodic changes of \mathbf{k} lead to a full winding of the phase (red circle). Contrary to this, in the trivial phase, $\theta(\mathbf{k})$ does not perform a full winding as a function of \mathbf{k} (the origin is outside of the Z_k trajectory). Panels from (b) to (d) show exemplary results for $\mu/t = -2, -1.25$, and -0.5 , respectively, for fixed $h/t = 0.5$, $\Delta/t = 0.2$ and $\lambda/t = 0.15$. TRIM ($\mathbf{k}_0 = 0$ and $\mathbf{k}_{\pm 1} = \pm\pi/2$) are depicted as white points. The behaviour of the winding number in the non-trivial phase is shown in panels (b) and (d). For the trivial phase z_k does not describe a closed unit circle.

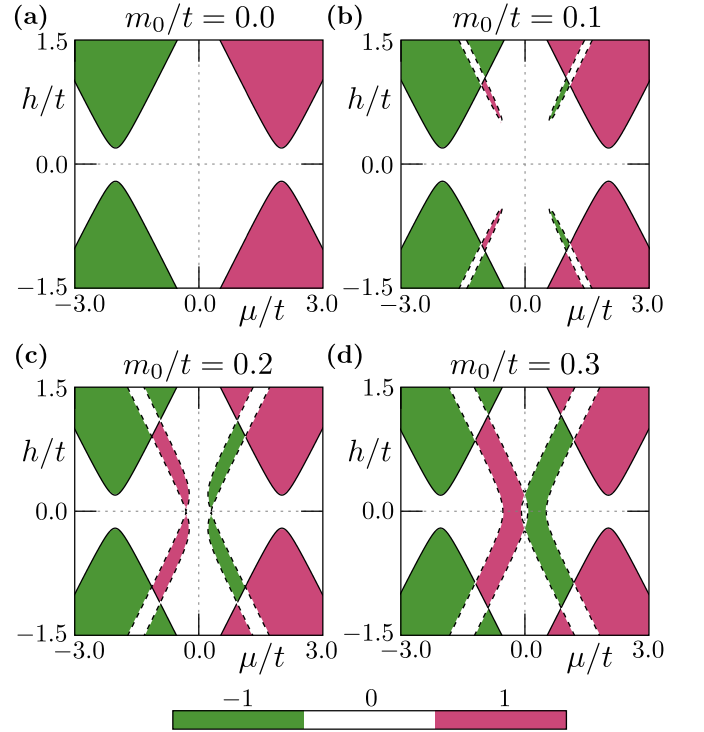


Figure 6. Topological phase diagrams obtained from the winding number w , given by Eq. (17), for different amplitudes of the AFM order m_0 (as labeled). Color denotes the trivial phase, $w = 0$, (white) and the non-trivial phases with $w = -1$ (green) and $w = 1$ (red). Solid black lines show gap closings at $k = 0$ and dashed lines show gap closings at $k = \pm\pi/2$. Results are for $\Delta/t = 0.2$ and $\lambda/t = 0.15$.

at the second TRIM $\pi/2$. When the magnitude of the AFM order m_0 is significantly large, additional topological branches emerge from main branches (along $|\mu| \approx |h|$ line) [cf. Fig. 6(a) and (b)]. If this occurs, for a range of parameters inside the main branches, the topological phase is destroyed as these phases have opposite chirality. Further increasing of m_0 joins the AFM branches and leads to a destructive overlap and emergence of a trivial phase around $\mu = h = 0$ [Fig. 6(d)]. When the AFM amplitude is relatively large, the non-trivial phase can exist around $\mu \approx 0$, i.e. in the nearly-half-filling limit $n \approx 1$ [cf. Fig. 6(c) and (d)].

Summarizing this part, the topological phase diagram is composed of two branches of the non-trivial phase — the main branch associated with TRIM at $\mathbf{k} = 0$ and the additional branch connected with the second TRIM at $\mathbf{k} = \pm\pi/2$. The main branch has properties which can be typically observed in the standard Rashba nanowire scenario, while the nontrivial phase originating in the additional branch can be compared to the nontrivial phase induced by dimerization [80].

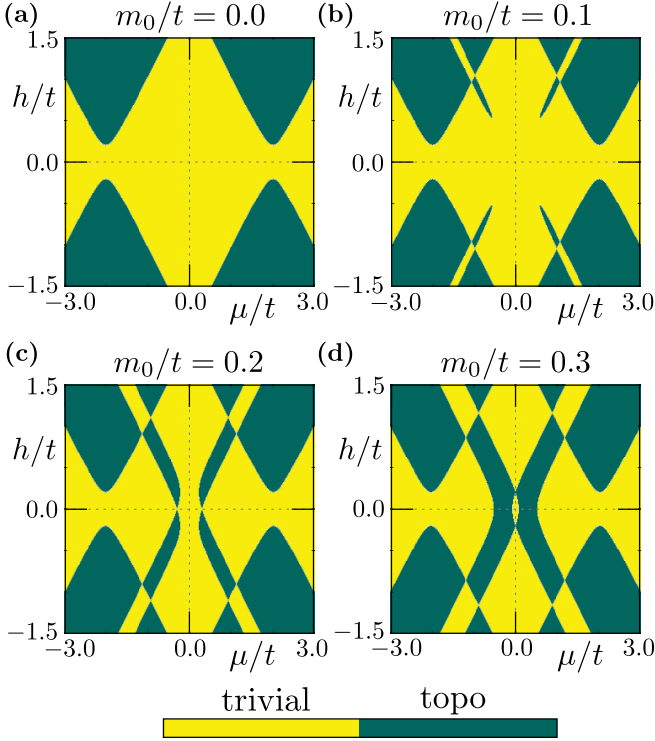


Figure 7. Topological phase diagrams, obtained from the topological index \mathcal{Q} calculated numerically using the S matrix method (cf. Sec. III C) for different amplitudes of the AFM order m_0 (as labeled). Color denotes trivial (yellow) and non-trivial (green) topological phase. Results from $\Delta/t = 0.2$ and $\lambda/t = 0.15$ for lattice with 200 sites without periodic boundary conditions.

C. Scattering matrix method

As an independent check of the preceding analytical calculations the behavior of the topological properties can be investigated by studying the scattering matrix S , which relates the incoming and outgoing wave amplitudes (further discussion on this point can be found in Sec. V) [81–85]. In this method, the \mathbb{Z}_2 topological quantum number can be found from $\mathcal{Q} = \text{sgn det } R$, where R denotes the reflection sub-matrix of S . The scattering matrix can be calculated exactly from the real space Hamiltonian in the frame of the transfer-matrix scheme, described in detail in Ref. [85–87]. Using this method, we evaluated the topological phase diagram numerically.

Topological phase diagrams found with this method are shown in Fig. 7. The (non-)trivial topological phase covers the (green) yellow regions. It can be seen that in the absence of the AFM order, the boundary of the non-trivial phase in the μ – h space, is given by the known characteristic parabolas [Fig. 7(a)]. The existence of the AFM order, modifies the boundaries of the non-trivial phase around diagonal lines $|\mu| \approx |h|$ [Fig. 7(b)], such a modification is a result of the presence of the sublattice in the system. These phase diagram were obtained numerically and are in complete agreement with the previous results obtained from analytical calculations (Fig. 6).

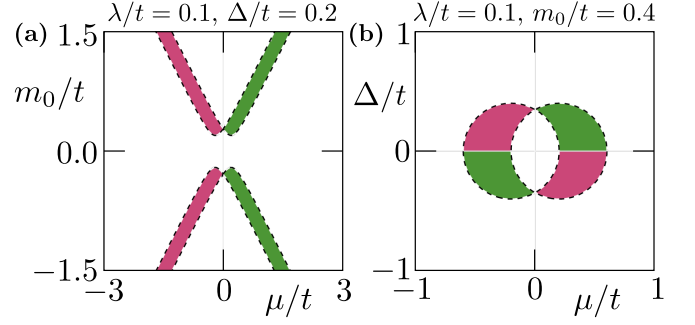


Figure 8. Topological phase diagram in the absence of the magnetic field. Results are shown as a function of the amplitude of the AFM order and chemical potential (a); and of the SC order and and chemical potential (b). The boundaries of the non-trivial topological phases are given by the dashed lines. The winding number w color scheme is as in Fig. 6. In panel (b) the circles are centered on $\pm 2\lambda$ with a radius $|m_0|$.

ically and are in complete agreement with the previous results obtained from analytical calculations (Fig. 6).

D. Majorana bound states without a Zeeman field

Analysis of these phase diagrams show important features of the described system: first with the increase of the amplitude of m_0 , we can see an emergence of additional *branches* of non-trivial phase. Moreover, for some range of parameters the non-trivial topological phase can emerge without any external magnetic field but instead, only due to the existence of the AFM order in the system. This is manifested in the additional branch of the topological phase caused by the band inversion at the $\mathbf{k} = \pi/2$ TRIM [cf. Fig. 6(d)].

Due to fact that the additional branch is connected with $\mathbf{k} = \pi/2$ TRIM, let us analyze the properties of $\text{Pf}[\mathcal{W}(\pi/2)]$ for $h = 0$. In this case $h_{\pm} = \pm m_0$, which gives

$$\text{Pf}[\mathcal{W}(\pi/2)]|_{h=0} = \left[\Delta^2 - m_0^2 + (\mu + 2\lambda)^2 \right] \times \left[\Delta^2 - m_0^2 + (\mu - 2\lambda)^2 \right]. \quad (27)$$

One should note that in the limit $\lambda \rightarrow 0$, we have

$$\text{Pf}[\mathcal{W}(\pi/2)] \rightarrow (m_0^2 - \mu^2 - \Delta^2)^2 \geq 0. \quad (28)$$

As we can see, SOC is still a mandatory ingredient of the non-trivial topological phase.

The impact of the AFM order amplitude and the SOC on the emergence of the non-trivial topological phase is shown in Fig. 8. Interestingly, the boundaries of the non-trivial topological phase are given exactly by two circles centered on $\pm 2\lambda$ with a radius $|m_0|$ [Fig. 8(b)]. When the circles overlap each other, the overlapping region is in the trivial phase (no coloring).

IV. ELECTRONIC PROPERTIES

In this section, we will discuss the electronic properties of the system. The numerical results presented in this section were obtained for a nanowire with $N = 200$ sites and fixed values of $\Delta/t = 0.2$ and $\lambda/t = 0.15$.

A. Topological gap and zero-energy states

In the absence of symmetry breaking, a topological phase transition from a trivial to a non-trivial phase is associated with closing of the trivial gap and reopening of a new topological gap. In the case of the system without periodic boundary conditions, i.e. with edges, the existence of MBS is equivalent to the existence of the nearly-zero-energy state after the phase transition to the non-trivial topological phase. However, a small value of the energy gap δE (defined as a difference between energies nearest to the Fermi level in the spectrum of the system) is not a good indicator of the existence of MBS (Fig. 9). Still, a substantial decrease of δE can indicate a clearly visible boundary between two topological phases, and has the advantage of being relatively straightforward to measure experimentally, in contrast to the invariants. For instance, in the absence of the AFM order [Fig. 9(a)],

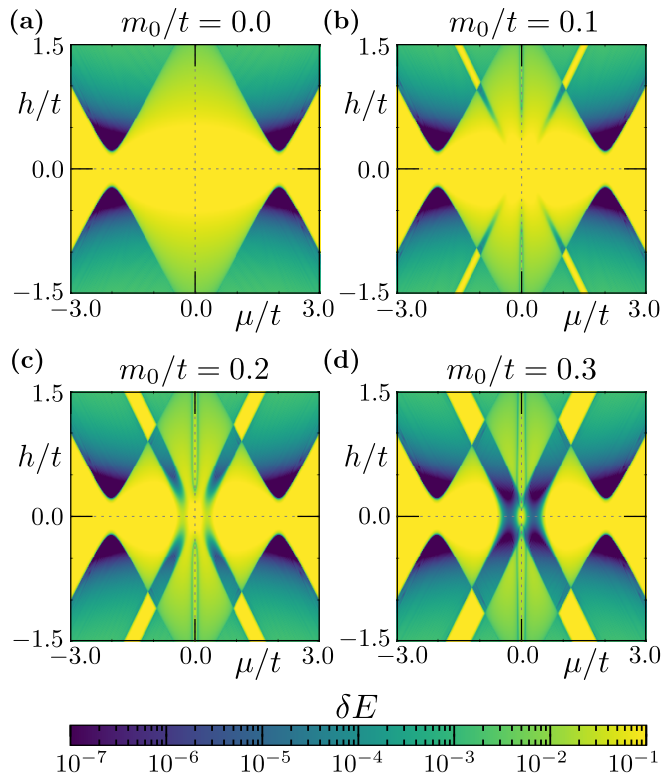


Figure 9. Values of the “gap” δE defined as the difference between the energies of the two eigenstates which are nearest to the Fermi level for different amplitudes of the AFM order m_0 (as labeled).

the phase boundary of the non-trivial topological phase is visible in the form of characteristic parabolas. An identical shape can be found in the corresponding topological phase diagram [cf. with Fig. 6(a)].

The phase diagrams prove to be more complicated in the presence of the AFM order. For some values of μ , we can observe additional regions with extremely small values of δE , e.g. vertical lines around $\mu/t = 0$ at Fig. 9(c) and (d). This behavior is associated with crossing of the Fermi level by the separate energy levels and can be noticed in the spectrum of the system [cf. red arrows at Fig. 10(a) and (b)]. Moreover, as these states exist in the trivial phase, they can not generate MBS at the end of the chain.

Energy spectra of the system are shown in Fig. 10. For half-filling (i.e. $\mu = 0$) some midgap states can cross the Fermi level $E = 0$ [shown by a red arrow in Fig. 10(a) and (b)]. However, a non-trivial topological phase is not present and these states are not MBS. In the non-trivial topological phase, MBS are visible in the spectrum of the system in the form of two close to degenerate zero-energy states (the range of h corresponding to the non-trivial

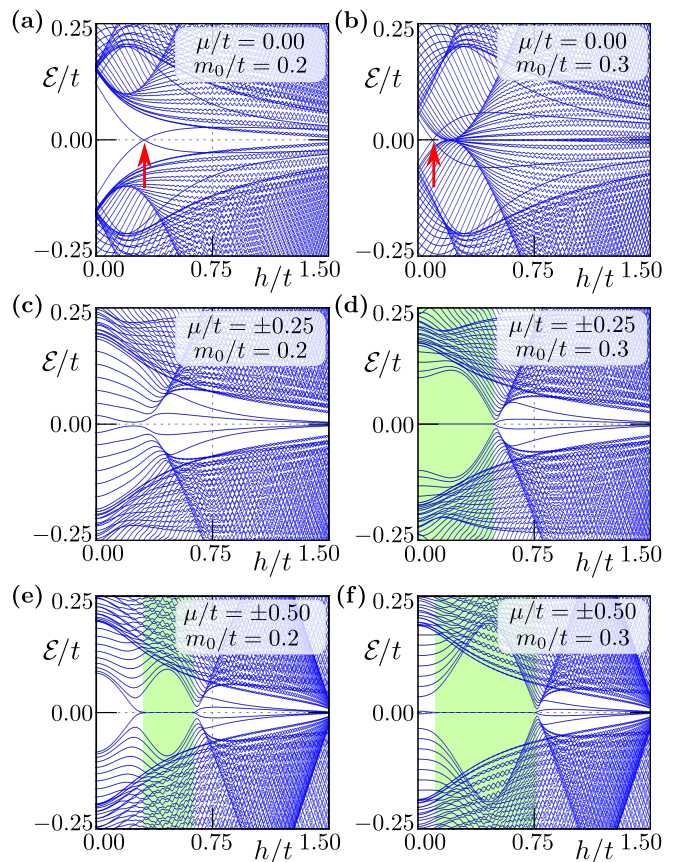


Figure 10. The spectrum of the system for various values of the chemical potential μ and the AFM amplitude m_0 (as labeled) as a function of the magnetic field h . The range of h marked by the green color corresponds with the non-trivial topological phase.

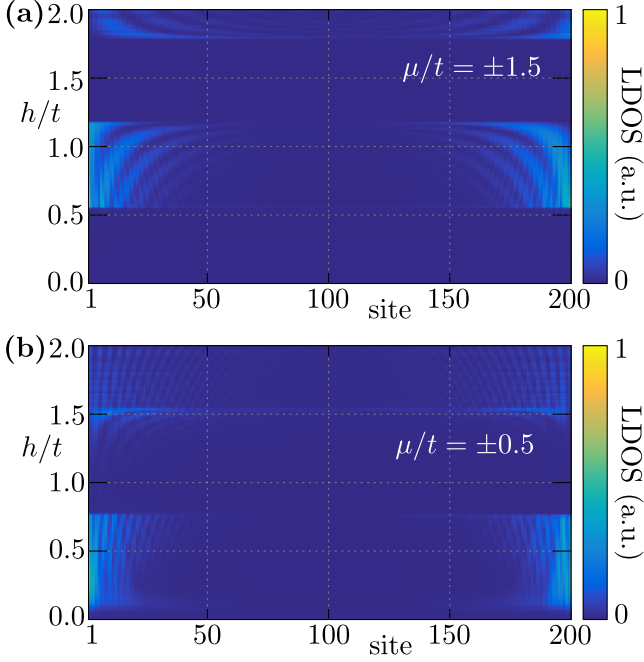


Figure 11. Zero-energy local density of states (LDOS) as a function of the magnetic field h . Results are for AFM order with an amplitude $m_0/t = 0.3$.

phase is marked by the green color in Fig. 10). Similar to the nanowire without AFM order, eigenvalues show oscillations as a function of magnetic field h [88, 89].

B. Localization of the Majorana modes

Localization of the Majorana states can be studied via the zero-energy LDOS (5). Exemplary results for several values of the chemical potential μ as the magnetic field h is increased are shown in Fig. 11. In each topological phase, independently of the topological branch, the MBS are well localized around each end of the chain. We can also observe the exponential decay of the MBS starting near the end of the chain and decaying to the middle. Moreover, for sufficiently high h , alternating oscillations of the Majorana bound states energies around the Fermi level are observed in the form of horizontal lines that represent the distribution of zero-energy states on the entire nanowire. The same behavior have been discussed in the context of the energy gap in the previous section. With increasing magnetic field, we can observe a series of topological phase transition from trivial to non-trivial and vice-versa as one would cross the branches of the topological phase diagram [cf. Fig. 6].

C. Influence of the sublattices

From a diagonalization of the Hamiltonian in real space (cf. Sec. II A) using the BdG formalism, in the non-trivial topological phase we can find two zero-energy fermionic modes Ψ^\pm at exponentially small energies $\pm\delta\epsilon$. From this, using a simple rotation:

$$\begin{pmatrix} \Psi_{is}^L \\ \Psi_{is}^R \end{pmatrix} = \frac{1}{\sqrt{2}} \begin{pmatrix} 1 & 1 \\ -i & i \end{pmatrix} \begin{pmatrix} \Psi_{is}^+ \\ \Psi_{is}^- \end{pmatrix}, \quad (29)$$

we can find Majorana modes localized exactly at the left Ψ^L or the right Ψ^R side of the chain. Note that $\Psi^{L/R}$ are eigenstates of the particle-hole operator and therefore represent true Majorana modes. Example results are show in Fig. 12, where left and right modes are show by green and orange solid lines, respectively.

We will focus our analysis on the Majorana bound states manifesting in the additional branch of the topological phase diagram. In the absence of the external magnetic field the site-dependent distribution of the particles with opposite spins $n_{i\sigma}$ is given only by the AFM order. The total average number of particles per site $\langle n \rangle = \sum_{i\sigma} n_{i\sigma}/2N$ is always fixed by the chemical potential. The distribution of particles with spin \uparrow and \downarrow has a reflection symmetry with respect to the center of the system. Average number of particles in each site is approximately constant, however the AFM order introduced a distinguishability of the sublattices via magnetization—in other words magnetization in sublattice A is different to B. Here, we should mention that the properties described above in the absence of the magnetic field do not depends on the parity of the number of sites.

The situation looks different in the presence of the magnetic field. In the case of the system with even number of sites [Fig. 12(a)], this leads to a loss of the reflection symmetry. This is a consequence of the modification of the $n_{i\sigma}$ distribution due to interplay between the AFM order and magnetic field. In fact, the effective magnetic field h_\pm at first and last site of the chain are not identical. The reflection symmetry can be recovered by elongating the nanowire by one site, what yields an odd total number of sites [Fig. 12(b)]. As a result, first and last site belong to the same sublattice (cf. the inset). Similar modification of the mirror symmetry by odd or even number of sites in the system is also observed in particle distributions. However, the bound states have only a very small influence on the particle distribution in the central region of the nanowire.

D. Spectral function analysis

The origin of the main and additional AFM branches in the topological phase diagram can be studied in the context of the spectral function:

$$\mathcal{A}_{\mathbf{k}}(\omega) = -\frac{1}{\pi} \sum_{s\sigma} \text{Im} G_{\mathbf{k}s\sigma}(\omega + i0^+), \quad (30)$$

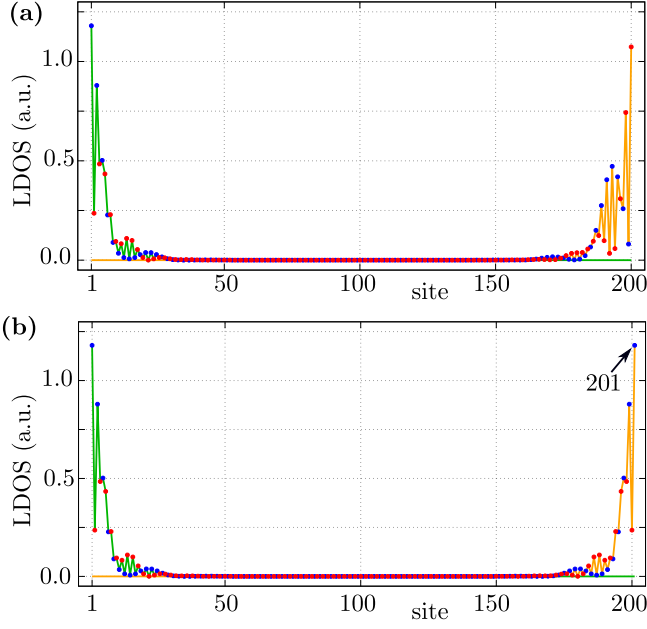


Figure 12. The zero-energy local density of states (LDOS) corresponding to the MBS. Blue and red dots represent the A and B sublattice sites, respectively. Results for $\mu/t = -0.3$, $h/t = 0.2$ and $m_0/t = 0.3$. A comparison of results for chains with (a) 200 and (b) 201 sites.

where $G_{\mathbf{k}\sigma\sigma} = \langle c_{\mathbf{k}\sigma\sigma} | (\omega - H)^{-1} | c_{\mathbf{k}\sigma\sigma}^\dagger \rangle$. In practice, the spectral function can be re-expressed in terms of the BdG coefficients:

$$\begin{aligned} \mathcal{A}_{\mathbf{k}}(\omega) &= \sum_{\mathbf{k}\sigma\sigma} \mathcal{A}_{\mathbf{k}\sigma\sigma} \\ &= \sum_{\mathbf{k}\sigma\sigma} [|u_{\mathbf{k}\sigma\sigma}^n|^2 \delta(\omega - \mathcal{E}_{\mathbf{k}n}) + |v_{\mathbf{k}\sigma\sigma}^n|^2 \delta(\omega + \mathcal{E}_{\mathbf{k}n})], \end{aligned} \quad (31)$$

where $u_{\mathbf{k}\sigma\sigma}^n$ and $v_{\mathbf{k}\sigma\sigma}^n$ are components of the n -th eigenvector of the Hamiltonian (11). Here we have introduced the sublattice- and spin-dependent spectral function $\mathcal{A}_{\mathbf{k}\sigma\sigma}$. The topological phase transition is associated with a band inversion during the transition. To study this behavior in our system we can define

$$\delta\mathcal{A}_{\mathbf{k}}^s = \mathcal{A}_{\mathbf{k}A\uparrow} + \mathcal{A}_{\mathbf{k}A\downarrow} - \mathcal{A}_{\mathbf{k}B\uparrow} - \mathcal{A}_{\mathbf{k}B\downarrow}, \quad (32)$$

$$\delta\mathcal{A}_{\mathbf{k}}^\sigma = \mathcal{A}_{\mathbf{k}A\uparrow} - \mathcal{A}_{\mathbf{k}A\downarrow} + \mathcal{A}_{\mathbf{k}B\uparrow} - \mathcal{A}_{\mathbf{k}B\downarrow}. \quad (33)$$

$\delta\mathcal{A}_{\mathbf{k}}^s$ and $\delta\mathcal{A}_{\mathbf{k}}^\sigma$ describe the imbalance in the sublattice and spin subspace at momentum \mathbf{k} respectively.

Let us start with an analysis of the spectral function in the case when the topological phase arises in the main branch of the topological phase diagram (Fig 14). As written previously, these topologically non-trivial phases occur due to the band gap closing at the TRIM $\mathbf{k} = 0$. Increasing the magnetic field, for fixed chemical potential, leads to a topological phase transition from the trivial to non-trivial phase. During this transition the band inversion is observed in both (sublattice and spin) subspaces. Before the topological phase transition, i.e. $h < h_c$, and

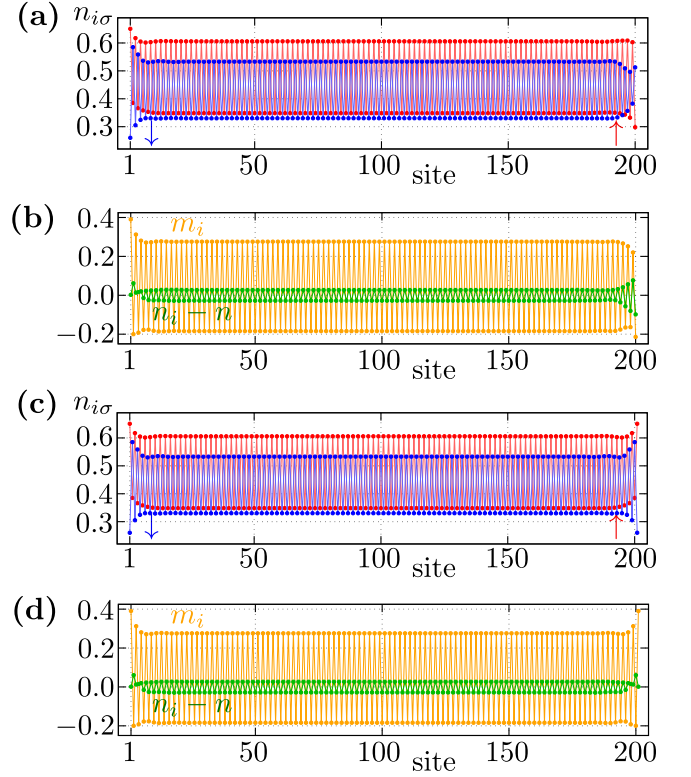


Figure 13. The distribution of particles $n_{i\sigma}$ with spin \uparrow (red) and \downarrow (blue) in the system, as well as magnetization m_i (orange) and the difference between the average number of particles on a particular site and the average number per site in the system as a whole, $n_i - n$ (green). A comparison of results for the chains with 200 [panels (a) and (b)] and 201 [panels (c) and (d)] sites is shown. Same parameters as Fig. 12 for $\mu/t = -0.3$, $h/t = 0.2$ and $m_0/t = 0.3$.

in both subspaces, we observe the order of the bands “polarization”: to be $(+, -, +, -)$, ordering from negative to positive energy [Fig 14(e) and (f)]. For the chosen parameters, topological phase transition occurs at the critical magnetic field $h_c/t \simeq 0.2$. When $h = h_c$, the gap is closed and two bands touch each other at $\mathbf{k} = 0$ [Fig 14(c) and (d)]. Further increase of h leads to a changing of the “polarization” order to $(+, +, -, -)$ at $\mathbf{k} = 0$ [Fig 14(a) and (b)]. At $\mathbf{k} = \pi/2$ the ordering remains $(+, -, +, -)$ and hence there is band inversion. This inversion occurs in both sublattice and spin subspaces at the same time. From this, we can conclude that the main branch of the topological phase emerges as an effect of the external magnetic field, independently of the AFM order.

Now, we turn to analyze the inversion of the bands in the case of the additional, AFM-related, branch of the topological phase diagram (Fig 15). In this case the existence of the topological phase is associated with the system properties at the TRIM $\mathbf{k} = \pm\pi/2$. As previously, increasing the magnetic field leads to the topological phase transition. However, during this transition, in the spin sector we do not observe band inversion, i.e. the

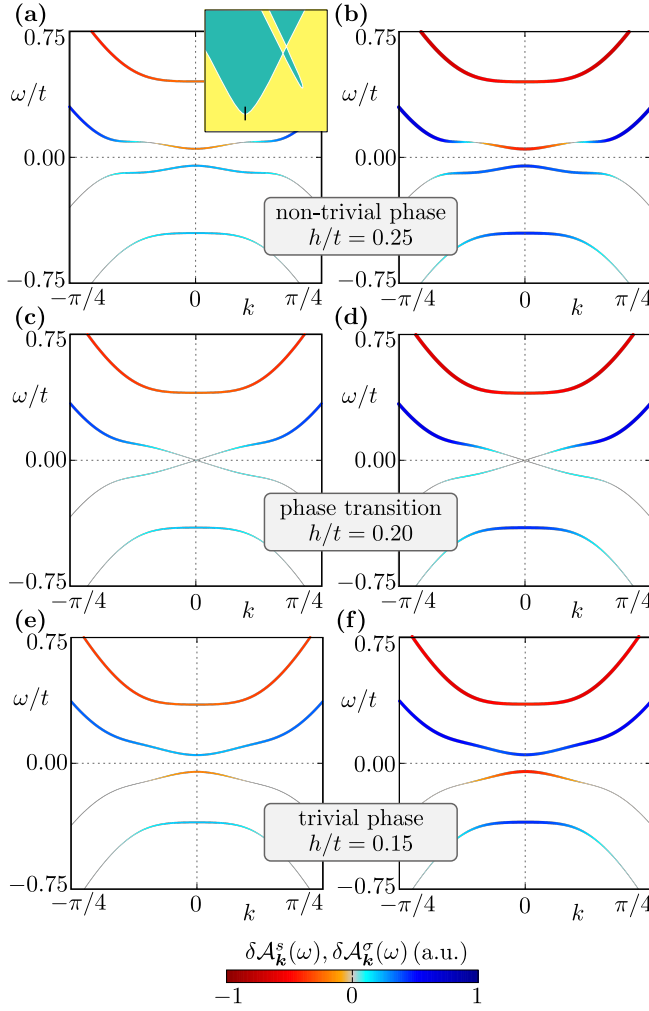


Figure 14. Distinctions in sublattice and spin dependent spectral functions, $\delta\mathcal{A}_{\mathbf{k}}^s(\omega)$ (left panels) and $\delta\mathcal{A}_{\mathbf{k}}^\sigma(\omega)$ (right panels). Results for $m_0/t = 0.1$, $\mu/t = -2.0$ and $h/t = 0.15, 0.20, 0.25$ (panels from bottom to top) – showing the topological phase transition from the trivial to the non-trivial topological phase along the main branch (the black line is not in scale, shown in the inset).

spin polarization for each band is the same and positive (Fig 15 right panels) – the spin imbalance in the system is unchanged due to the presence of a relatively strong magnetic field. The situation looks different in the sublattice sector. In the trivial phase [Fig 15(e)], we observe band ordering as in the previous case, i.e. $(+, -, +, -)$. At $h = h_c$, we observe a closing of the gap at the TRIM $\mathbf{k} = \pi/2$ [Fig 15(f)]. A further increase of h leads to a band inversion in sublattice frame and the polarization order $- (+, +, -, -)$ at $\mathbf{k} = \pi/2$. From this we can conclude, that the key role of AFM order is key in the emergence of the additional branch in the topological phase diagram. Moreover, the introduction of the sublattice imbalance by the AFM order is the main source of the non-trivial band topology.

Band inversion is a very typical signature of a topo-

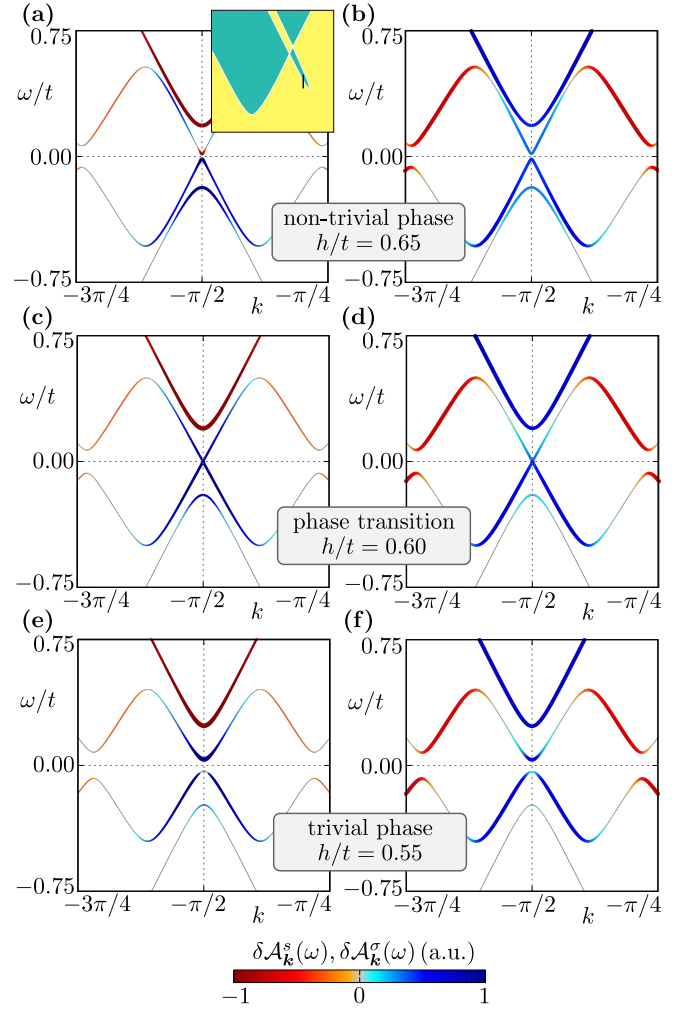


Figure 15. Distinctions in sublattice and spin dependent spectral function, $\delta\mathcal{A}_{\mathbf{k}}^s(\omega)$ (left panels) and $\delta\mathcal{A}_{\mathbf{k}}^\sigma(\omega)$ (right panels), respectively. Results for $m_0/t = 0.1$, $\mu/t = -0.7$ and h/t equal 0.55, 0.60, and 0.65 (panels from bottom to top) – topological phase transition from trivial to non-trivial topological phase along additional branch (the green line is not in scale, shown at inset).

logical phase transition in these systems [90–92], and was also reported as a signature of the topological phase transition in the case of the Rashba chain [29, 93]. The spectral function can be measured in angle-resolved photoemission spectroscopy (ARPES) experiments [62]. The properties described above open a new way for the experimental examination of the construction of the additional topological branches in the AFM chain, and their comparison with the standard branch.

V. TRANSPORT PROPERTIES

Here, we show the results of numerical calculations of the differential conductance of the studied system using the scattering formalism [81–85]. Our system, can

be treated as a superconducting chain connected to normal leads (cf. Fig. 16), i.e. and N/S/N junction. Then the scattering matrix relating all incident and outgoing modes in this system is:

$$S = \begin{pmatrix} S_{11} & S_{12} \\ S_{21} & S_{22} \end{pmatrix}, \quad S_{ij} = \begin{pmatrix} S_{ij}^{ee} & S_{ij}^{eh} \\ S_{ij}^{he} & S_{ij}^{hh} \end{pmatrix}. \quad (34)$$

The S_{ij}^{ab} is the block of scattering amplitudes of incident particles of type b in lead j to particles of type a in lead i [84]. The zero-temperature differential conductance matrix is

$$G_{ij}(E) \equiv \frac{\partial I_i}{\partial V_j} = G_0 (T_{ij}^{ee} - T_{ij}^{he} - \delta_{ij} N_i^e), \quad (35)$$

where I_i is the current entering terminal i from the scattering region, while V_j is the voltage applied to terminal j . Here $G_0 = e^2/\hbar$ is the conductance quantum without the spin degeneracy taken into account. N_i^e is the number of electron modes at energy E in terminal i . The energy transmission is given as

$$T_{ij}^{ab} = \text{Tr} \left([S_{ij}^{ab}]^\dagger S_{ij}^{ab} \right). \quad (36)$$

We performed the calculation in the case of the N/S/N system shown in Fig. 16, using the KWANT [94] code to numerically obtain the scattering matrix.

An experimental study of the MBS emergence in the system can be performed by local differential conductance G_{ii} measurements (for $i = 1, 2$). In the tunneling regime, the local conductance G_{ii} in a normal lead probes the density of states in the proximitized region. From this, one can obtain information about the in-gap states close to the i -th normal lead. In a typical situation, the local conductance G_{ii} is quantized by G_0 [95] (if spin degeneracy is not present). However, for “true” zero energy bound states, the local conductance G_{ii} should be equal to $2G_0$ (per each MBS) [96–98]. A measurement of G_{ii} in such a case can yield important information about the existence of the MBS and can be used in the experimental “testing” of the topological phase diagram [99]. Contrary to this, non-local conductance G_{12} (or G_{21}) can give information about the non-trivial topological gap [84, 100] and be helpful in distinguishing between non-trivial in-gap states and the “bulk” states. The induced gap matches the energies at which the non-local conductance becomes finite [84].

First, we evaluate the local G_{11} and non-local G_{12} conductance for several fixed values of chemical potential μ



Figure 16. Schematic representation of system used in the differential conductance G calculation — AFM chain connected to two normal leads. Due to the Coulomb blockade between leads and chains, a barrier region exists in the system (gray area).

and magnetic field h (Fig. 17). We assume $m_0/t = 0.3$, which corresponds to a rich topological phase diagram, cf. Fig. 17(a). In the simplest case, in the absence of the magnetic field, for chemical potential near the bottom of band ($\mu/t = -2$), i.e. Fig. 17(b), G_{11} takes maximal values around G_0 , while G_{12} correctly shows the value of the gap (marked by the shaded orange background). The transition to the topological phase by increasing the magnetic field leads to the emergence of MBS associated with the zero-bias peak of $G_{11} = 2G_0$, cf. Fig. 17(b). At the same time, non-zero value of G_{12} show induced topological gap. In the intermediate trivial region, Fig. 17(c) for $\mu/t = 1.5$ and $h/t = 1.25$, the results look similar to the first case. Results obtained within the additional branch of the topological phase diagram, i.e. Fig. 17(e), look similar to the main branch — G_{12} indicate the values of the small topological gap with clearly visible zero-bias MBS peak $G_{11} = 2G_0$. Finally, going to the central trivial region of the phase diagram, for $\mu/t = 0$ and $h/t = 0$, i.e. Fig. 17(f), again a typical signature of the trivial phase can be seen. Additionally, due to the closeness to the boundary of the topological phase, we observe a signature of the extremely small gap in G_{12} .

Analogously to the experimental venue [99], we can try to reproduce the shape of the topological phase di-

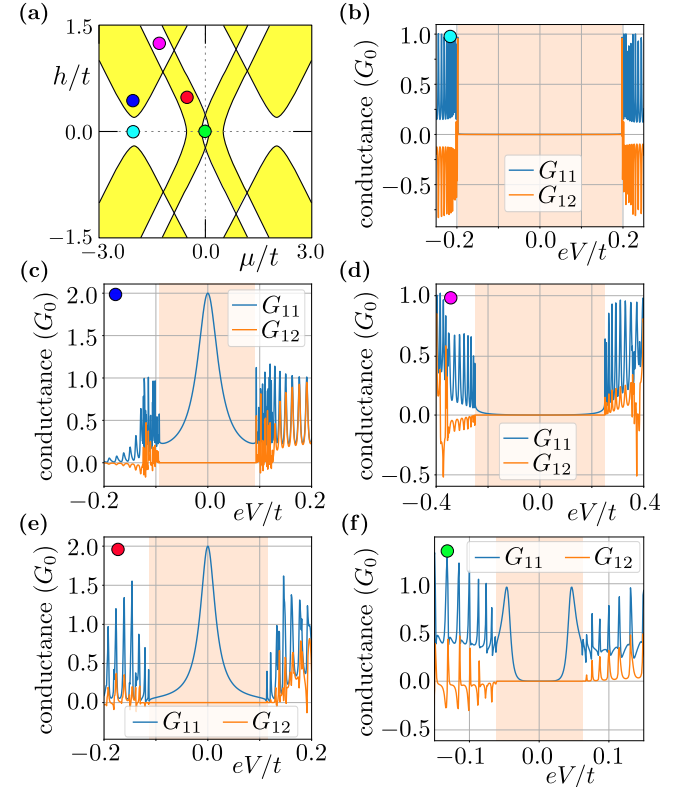


Figure 17. Local (G_{11}) and non-local (G_{12}) differential conductance for different sets of the system parameters μ and h (marked by color points). Results for a finite size chain with 200 sites and fixed $m_0/t = 0.3$, $\Delta/t = 0.2$ and $\lambda/t = 0.15$.

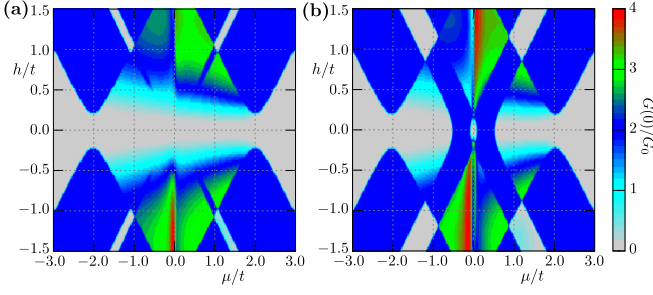


Figure 18. Value of the zero-bias local differential conductance $G_{11}(0)$ in the case of AFM nanowire with $m_0/t = 0.1$ (a) and $m_0/t = 0.3t$ (b). Results for finite chain with 200 sites, $\Delta/t = 0.2$, and $\lambda/t = 0.15$.

agram by studying the zero-bias local conductance G_{11} (Fig. 18). The conductance quanta $2G_0$ (the blue color) reproduce the main features of the topological phase diagram. As the calculations have been performed for a finite size system, we observe a vanishing of the MBS in some parts of diagram, similar to the situation previously described in Sec. III. Parallel contours are characteristic for a system with finite size [101] and associated with splitting of the in-gap energies [102]. The amplitude of such oscillations can be reduced by the increase of the nanowire length [30], i.e. by the number of sites in the nanowire.

VI. SUMMARY

In this paper, we studied the possibility of the emergence of Majorana bound states in a nanowire with antiferromagnetic and superconducting order induced by proximity effects. We found that the topological phase diagram is composed of two branches of the non-trivial topological phase. The main branch has the typical properties characteristic for a superconducting Rashba nanowire, while the second additional branch is associated with the existence of the antiferromagnetic order. Moreover, for some range of the parameters, the additional branch of the non-trivial topological phase can “survive” even in the absence of the external magnetic field. In such a case, antiferromagnetic order is the source of the non-trivial phase near the half-filling limit.

These results show an emergence of a new, antiferromagnetic topological phase that can be contrasted with the typical situation, when the Majorana bound states

can emerge only if the density of the particles is sufficiently low (i.e. when the Fermi level is located near the bottom of the band) and the system is under the effect of an external magnetic field. However, the phase transition to the non-trivial topological phase can still induced by the external magnetic field or by changing of the chemical potential, i.e. by doping. We show that the standard non-trivial phase of such a nanowire has a different band inversion signature to that of the novel phase, which could be measured in ARPES experiments. We also explored experimental signatures of the MBS and topological gap in the local and non-local differential conductance.

ACKNOWLEDGMENTS

We kindly thank Pascal Simon for fruitful discussions. This work was supported by the National Science Centre (NCN, Poland) under the grants UMO-2018/31/N/ST3/01746 (A.K.), UMO-2018/29/B/ST3/01892 (N.S.), and UMO-2017/24/C/ST3/00276 (A.P.).

Appendix A: Real space Bogoliubov–de Gennes Hamiltonian

The real space Bogoliubov–de Gennes (BdG) equations, can be written in the form $\mathcal{E}_n \Psi_{isn} = \mathbb{H}_{is,j s'} \Psi_{j s' n}$, where $\mathbb{H}_{is,j s'}$ is the Hamiltonian in the matrix form:

$$\mathbb{H}_{is,j s'} = \begin{pmatrix} H_{is,j s', \uparrow} & S_{is,j s'}^{\uparrow \downarrow} & \Delta_{is,j s'} & 0 \\ S_{is,j s'}^{\downarrow \uparrow} & H_{is,j s', \downarrow} & 0 & \Delta_{is,j s'} \\ \Delta_{is,j s'}^* & 0 & -H_{is,j s', \downarrow}^* & -S_{is,j s'}^{\downarrow \uparrow} \\ 0 & \Delta_{is,j s'}^* & -S_{is,j s'}^{\uparrow \downarrow} & -H_{is,j s', \uparrow}^* \end{pmatrix}, \quad (\text{A1})$$

with the eigenvectors

$$\Psi_{isn} = (u_{isn\uparrow}, u_{isn\downarrow}, v_{isn\downarrow}, v_{isn\uparrow})^T. \quad (\text{A2})$$

For the considered model (cf. Sec. II A), the matrix block elements, are given by $H_{is,j s', \sigma} = -t\delta_{ij}\delta_{\langle ss' \rangle} - t\delta_{i-1,j}\delta_{\langle ss' \rangle} - [\mu + \sigma(h + m_0(\delta_{sA} - \delta_{sB}))]\delta_{ij}\delta_{ss'}$, the superconductivity is denoted by $\Delta_{is,j s'} = \Delta\delta_{ij}\delta_{ss'}$ and $S_{is,j s'}^{\sigma\sigma'} = -i\lambda(\sigma_y)_{\sigma\sigma'}(\delta_{ij}\delta_{\langle ss' \rangle} - \delta_{i-1,j}\delta_{\langle ss' \rangle})$ gives the spin-orbit term.

-
- [1] A. Y. Kitaev, “Unpaired majorana fermions in quantum wires,” *Phys.-Usp.* **44**, 131 (2001).
 - [2] R. Aguado, “Majorana quasiparticles in condensed matter,” *La Rivista del Nuovo Cimento* **40**, 523 (2017).
 - [3] R. M. Lutchyn, E. P. A. M. Bakkers, L. P. Kouwenhoven, P. Krogstrup, C. M. Marcus, and Y. Oreg, “Ma-

- jorana zero modes in superconductor-semiconductor heterostructures,” *Nat. Rev. Mater.* **3**, 52 (2018).
- [4] R. Pawlak, S. Hoffman, J. Klinovaja, D. Loss, and E. Meyer, “Majorana fermions in magnetic chains,” *Prog. Part. Nucl. Phys.* **107**, 1 (2019).

- [5] Ch. Nayak, S. H. Simon, A. Stern, M. Freedman, and S. Das Sarma, “Non-Abelian anyons and topological quantum computation,” *Rev. Mod. Phys.* **80**, 1083 (2008).
- [6] M. T. Deng, C. L. Yu, G. Y. Huang, M. Larsson, P. Caroff, and H. Q. Xu, “Anomalous zero-bias conductance peak in a Nb–InSb nanowire–Nb hybrid device,” *Nano Lett.* **12**, 6414 (2012).
- [7] V. Mourik, K. Zuo, S. M. Frolov, S. R. Plissard, E. P. A. M. Bakkers, and L. P. Kouwenhoven, “Signatures of Majorana fermions in hybrid superconductor-semiconductor nanowire devices,” *Science* **336**, 1003 (2012).
- [8] A. Das, Y. Ronen, Y. Most, Y. Oreg, M. Heiblum, and H. Shtrikman, “Zero-bias peaks and splitting in an Al–InAs nanowire topological superconductor as a signature of Majorana fermions,” *Nat. Phys.* **8**, 887 (2012).
- [9] A. D. K. Finck, D. J. Van Harlingen, P. K. Mohseni, K. Jung, and X. Li, “Anomalous modulation of a zero-bias peak in a hybrid nanowire-superconductor device,” *Phys. Rev. Lett.* **110**, 126406 (2013).
- [10] F. Nichele, A. C. C. Drachmann, A. M. Whiticar, E. C. T. O’Farrell, H. J. Suominen, A. Fornieri, T. Wang, G. C. Gardner, C. Thomas, A. T. Hatke, P. Krogstrup, M. J. Manfra, K. Flensberg, and Ch. M. Marcus, “Scaling of Majorana zero-bias conductance peaks,” *Phys. Rev. Lett.* **119**, 136803 (2017).
- [11] Ö. Gül, H. Zhang, J. D. S. Bommer, M. W. A. de Moor, D. Car, S. R. Plissard, E. P. A. M. Bakkers, A. Geresdi, K. Watanabe, T. Taniguchi, and L. P. Kouwenhoven, “Ballistic Majorana nanowire devices,” *Nat. Nanotech.* **13**, 192 (2018).
- [12] M. T. Deng, S. Vaitiekėnas, E. B. Hansen, J. Danon, M. Leijnse, K. Flensberg, J. Nygård, P. Krogstrup, and C. M. Marcus, “Majorana bound state in a coupled quantum-dot hybrid-nanowire system,” *Science* **354**, 1557 (2016).
- [13] M.-T. Deng, S. Vaitiekėnas, E. Prada, P. San-Jose, J. Nygård, P. Krogstrup, R. Aguado, and C. M. Marcus, “Nonlocality of Majorana modes in hybrid nanowires,” *Phys. Rev. B* **98**, 085125 (2018).
- [14] S. Nadj-Perge, I. K. Drozdov, J. Li, H. Chen, S. Jeon, J. Seo, A. H. MacDonald, B. A. Bernevig, and A. Yazdani, “Observation of Majorana fermions in ferromagnetic atomic chains on a superconductor,” *Science* **346**, 602 (2014).
- [15] R. Pawlak, M. Kisiel, J. Klinovaja, T. Meier, S. Kawai, T. Glatzel, D. Loss, and E. Meyer, “Probing atomic structure and Majorana wavefunctions in mono-atomic Fe chains on superconducting Pb surface,” *Npj Quantum Information* **2**, 16035 (2016).
- [16] B. E. Feldman, M. T. Randeria, J. Li, S. Jeon, Y. Xie, Z. Wang, I. K. Drozdov, B. A. Bernevig, and A. Yazdani, “High-resolution studies of the Majorana atomic chain platform,” *Nat. Phys.* **13**, 286 (2016).
- [17] M. Ruby, B. W. Heinrich, Y. Peng, F. von Oppen, and K. J. Franke, “Exploring a proximity-coupled Co chain on Pb(110) as a possible Majorana platform,” *Nano Lett.* **17**, 4473 (2017).
- [18] S. Jeon, Y. Xie, J. Li, Z. Wang, B. A. Bernevig, and A. Yazdani, “Distinguishing a Majorana zero mode using spin-resolved measurements,” *Science* **358**, 772 (2017).
- [19] H. Kim, A. Palacio-Morales, T. Posske, L. Rózsa, K. Palotás, L. Szunyogh, M. Thorwart, and R. Wiesendanger, “Toward tailoring Majorana bound states in artificially constructed magnetic atom chains on elemental superconductors,” *Sci. Adv.* **4**, eaar5251 (2018).
- [20] B. Braunecker and P. Simon, “Interplay between classical magnetic moments and superconductivity in quantum one-dimensional conductors: Toward a self-sustained topological Majorana phase,” *Phys. Rev. Lett.* **111**, 147202 (2013).
- [21] J. Klinovaja, P. Stano, A. Yazdani, and D. Loss, “Topological superconductivity and Majorana fermions in RKKY systems,” *Phys. Rev. Lett.* **111**, 186805 (2013).
- [22] M. M. Vazifeh and M. Franz, “Self-organized topological state with Majorana fermions,” *Phys. Rev. Lett.* **111**, 206802 (2013).
- [23] B. Braunecker and P. Simon, “Self-stabilizing temperature-driven crossover between topological and nontopological ordered phases in one-dimensional conductors,” *Phys. Rev. B* **92**, 241410(R) (2015).
- [24] V. Kaladzhyan, P. Simon, and M. Trif, “Controlling topological superconductivity by magnetization dynamics,” *Phys. Rev. B* **96**, 020507(R) (2017).
- [25] G. M. Andolina and P. Simon, “Topological properties of chains of magnetic impurities on a superconducting substrate: Interplay between the Shiba band and ferromagnetic wire limits,” *Phys. Rev. B* **96**, 235411 (2017).
- [26] M. Sato, Y. Takahashi, and S. Fujimoto, “Non-Abelian topological order in *s*-wave superfluids of ultracold fermionic atoms,” *Phys. Rev. Lett.* **103**, 020401 (2009).
- [27] M. Sato and S. Fujimoto, “Topological phases of non-centrosymmetric superconductors: Edge states, Majorana fermions, and non-Abelian statistics,” *Phys. Rev. B* **79**, 094504 (2009).
- [28] M. Sato, Y. Takahashi, and S. Fujimoto, “Non-Abelian topological orders and Majorana fermions in spin-singlet superconductors,” *Phys. Rev. B* **82**, 134521 (2010).
- [29] A. Kobińska and A. Ptok, “Electrostatic formation of the Majorana quasiparticles in the quantum dot-nanoring structure,” *J. Phys.: Condens. Matter* **31**, 185302 (2019).
- [30] J. Klinovaja and D. Loss, “Composite Majorana fermion wave functions in nanowires,” *Phys. Rev. B* **86**, 085408 (2012).
- [31] C. Fleckenstein, F. Domínguez, N. Traverso Ziani, and B. Trauzettel, “Decaying spectral oscillations in a majorana wire with finite coherence length,” *Phys. Rev. B* **97**, 155425 (2018).
- [32] L. P. Gor’kov and E. I. Rashba, “Superconducting 2d system with lifted spin degeneracy: Mixed singlet-triplet state,” *Phys. Rev. Lett.* **87**, 037004 (2001).
- [33] K. Seo, L. Han, and C. A. R. Sá de Melo, “Topological phase transitions in ultracold Fermi superfluids: The evolution from Bardeen-Cooper-Schrieffer to Bose-Einstein-condensate superfluids under artificial spin-orbit fields,” *Phys. Rev. A* **85**, 033601 (2012).
- [34] A. Ptok, K. Rodríguez, and K. J. Kapcia, “Superconducting monolayer deposited on substrate: Effects of the spin-orbit coupling induced by proximity effects,” *Phys. Rev. Materials* **2**, 024801 (2018).
- [35] M. M. Desjardins, L. C. Contamin, M. R. Delbecq, M. C. Dartailh, L. E. Bruhat, T. Cubaynes, J. J. Viennot, F. Mallet, S. Rohart, A. Thiaville, A. Cottet, and T. Kontos, “Synthetic spin-orbit interaction for majorana

- rana devices,” *Nat. Mat.* **18**, 1060 (2019).
- [36] A. Yazdani, “Conjuring Majorana with synthetic magnetism,” *Nat. Mat.* **18**, 1036 (2019).
- [37] J. Klinovaja, P. Stano, and D. Loss, “Transition from fractional to Majorana fermions in Rashba nanowires,” *Phys. Rev. Lett.* **109**, 236801 (2012).
- [38] M. Kjaergaard, K. Wölms, and K. Flensberg, “Majorana fermions in superconducting nanowires without spin-orbit coupling,” *Phys. Rev. B* **85**, 020503(R) (2012).
- [39] J. Klinovaja and D. Loss, “Giant spin-orbit interaction due to rotating magnetic fields in graphene nanoribbons,” *Phys. Rev. X* **3**, 011008 (2013).
- [40] L.N. Maurer, J.K. Gamble, L. Tracy, S. Eley, and T.M. Lu, “Designing nanomagnet arrays for topological nanowires in silicon,” *Phys. Rev. Applied* **10**, 054071 (2018).
- [41] K. R. Sapkota, S. Eley, E. Bussmann, C. T. Harris, L. N. Maurer, and T. M. Lu, “Creation of nanoscale magnetic fields using nano-magnet arrays,” *AIP Advances* **9**, 075203 (2019).
- [42] V. Kornich, M. G. Vavilov, M. Friesen, M. A. Eriksson, and S. N. Coppersmith, “Majorana bound states in nanowire-superconductor hybrid systems in periodic magnetic fields,” *Phys. Rev. B* **101**, 125414 (2020).
- [43] T. Zhou, N. Mohanta, J. E. Han, A. Matos-Abiague, and I. Žutić, “Tunable magnetic textures in spin valves: From spintronics to Majorana bound states,” *Phys. Rev. B* **99**, 134505 (2019).
- [44] A. Matos-Abiague, J. Shabani, A. D. Kent, G. L. Fatin, B. Scharf, and I. Žutić, “Tunable magnetic textures: From Majorana bound states to braiding,” *Solid State Commun.* **262**, 1 (2017).
- [45] N. Mohanta, T. Zhou, J.-W. Xu, J. E. Han, A. D. Kent, J. Shabani, I. Žutić, and A. Matos-Abiague, “Electrical control of Majorana bound states using magnetic stripes,” *Phys. Rev. Applied* **12**, 034048 (2019).
- [46] L. Zhou, J. Wiebe, S. Lounis, E. Vedmedenko, F. Meier, S. Blügel, P. H. Dederichs, and R. Wiesendanger, “Strength and directionality of surface Ruderman-Kittel-Kasuya-Yosida interaction mapped on the atomic scale,” *Nat. Phys.* **6**, 187 (2010).
- [47] M. Menzel, Y. Mokrousov, R. Wieser, J. E. Bickel, E. Vedmedenko, S. Blügel, S. Heinze, K. von Bergmann, A. Kubetzka, and R. Wiesendanger, “Information transfer by vector spin chirality in finite magnetic chains,” *Phys. Rev. Lett.* **108**, 197204 (2012).
- [48] J. Hermenau, S. Brinker, M. Marciani, M. Steinbrecher, M. dos Santos Dias, R. Wiesendanger, S. Lounis, and J. Wiebe, “Stabilizing spin systems via symmetrically tailored RKKY interactions,” *Nat. Commun.* **10**, 2565 (2019).
- [49] S. Loth, S. Baumann, Ch. P. Lutz, D. M. Eigler, and A. J. Heinrich, “Bistability in atomic-scale antiferromagnets,” *Science* **335**, 196 (2012).
- [50] S. Yan, L. Malavolti, J. A. J. Burgess, A. Droghetti, A. Rubio, and S. Loth, “Nonlocally sensing the magnetic states of nanoscale antiferromagnets with an atomic spin sensor,” *Sci. Adv.* **3**, e1603137 (2017).
- [51] L. Pedrero, M. Brando, C. Klingner, C. Krellner, C. Geibel, and F. Steglich, “H-T phase diagram of YbCo_2Si_2 with H // [100],” *J. Phys.: Conf. Ser.* **200**, 012157 (2010).
- [52] T. Kong, S. Guo, D. Ni, and R. J. Cava, “Crystal structure and magnetic properties of the layered van der Waals compound VBr_3 ,” *Phys. Rev. Materials* **3**, 084419 (2019).
- [53] L. Hu, X. Wu, and J. Yang, “ Mn_2C monolayer: a 2D antiferromagnetic metal with high Néel temperature and large spin-orbit coupling,” *Nanoscale* **8**, 12939 (2016).
- [54] K. Kim, S. Y. Lim, J.-U. Lee, S. Lee, T. Y. Kim, K. Park, G. S. Jeon, Ch.-H. Park, J.-G. Park, and H. Cheong, “Suppression of magnetic ordering in XXZ-type antiferromagnetic monolayer NiPS_3 ,” *Nat. Commun.* **10**, 345 (2019).
- [55] M. Nakanishi, K. Yoshimura, K. Kosuge, T. Goto, T. Fujii, and J. Takada, “Anomalous field-induced magnetic transitions in V_5X_8 (X=S,Se),” *J. Magn. Magn. Mater.* **221**, 301 (2000).
- [56] W. J. Hardy, J. Yuan, H. Guo, P. Zhou, J. Lou, and D. Natelson, “Thickness-dependent and magnetic-field-driven suppression of antiferromagnetic order in thin V_5S_8 single crystals,” *ACS Nano* **10**, 5941–5946 (2016).
- [57] A. Heimes, P. Kotetes, and G. Schön, “Majorana fermions from Shiba states in an antiferromagnetic chain on top of a superconductor,” *Phys. Rev. B* **90**, 060507(R) (2014).
- [58] A. Heimes, D. Mendler, and P. Kotetes, “Interplay of topological phases in magnetic adatom-chains on top of a Rashba superconducting surface,” *New J. Phys.* **17**, 023051 (2015).
- [59] B. Kiczek and A. Ptok, “Influence of the orbital effects on the Majorana quasi-particles in a nanowire,” *J. Phys.: Condens. Matter* **29**, 495301 (2017).
- [60] P. G. de Gennes, *Superconductivity of metals and alloys* (Addison-Wesley, 1989).
- [61] A. V. Balatsky, I. Vekhter, and J.-X. Zhu, “Impurity-induced states in conventional and unconventional superconductors,” *Rev. Mod. Phys.* **78**, 373 (2006).
- [62] H. Matsui, T. Sato, T. Takahashi, S.-C. Wang, H.-B. Yang, H. Ding, T. Fujii, T. Watanabe, and A. Matsuda, “BCS-like Bogoliubov quasiparticles in high- T_c superconductors observed by angle-resolved photoemission spectroscopy,” *Phys. Rev. Lett.* **90**, 217002 (2003).
- [63] W. A. Hofer, A. S. Foster, and A. L. Shluger, “Theories of scanning probe microscopes at the atomic scale,” *Rev. Mod. Phys.* **75**, 1287 (2003).
- [64] R. Wiesendanger, “Spin mapping at the nanoscale and atomic scale,” *Rev. Mod. Phys.* **81**, 1495 (2009).
- [65] H. Oka, O. O. Brovko, M. Corbetta, V. S. Stepanyuk, D. Sander, and J. Kirschner, “Spin-polarized quantum confinement in nanostructures: Scanning tunneling microscopy,” *Rev. Mod. Phys.* **86**, 1127 (2014).
- [66] J. Stenger and T. D. Stanescu, “Tunneling conductance in semiconductor-superconductor hybrid structures,” *Phys. Rev. B* **96**, 214516 (2017).
- [67] R. S. K. Mong and V. Shivamoggi, “Edge states and the bulk-boundary correspondence in Dirac Hamiltonians,” *Phys. Rev. B* **83**, 125109 (2011).
- [68] T. Fukui, K. Shiozaki, T. Fujiwara, and S. Fujimoto, “Bulk-edge correspondence for Chern topological phases: A viewpoint from a generalized index theorem,” *J. Phys. Soc. Jpn.* **81**, 114602 (2012).
- [69] J. E. Moore and L. Balents, “Topological invariants of time-reversal-invariant band structures,” *Phys. Rev. B* **75**, 121306(R) (2007).

- [70] C. Dutreix, “Topological spin-singlet superconductors with underlying sublattice structure,” *Phys. Rev. B* **96**, 045416 (2017).
- [71] V. Baltz, A. Manchon, M. Tsoi, T. Moriyama, T. Ono, and Y. Tserkovnyak, “Antiferromagnetic spintronics,” *Rev. Mod. Phys.* **90**, 015005 (2018).
- [72] D. Bercioux and P. Lucignano, “Quantum transport in rashba spin-orbit materials: a review,” *Rep. Prog. Phys.* **78**, 106001 (2015).
- [73] A. Manchon, H. C. Koo, J. Nitta, S. M. Frolov, and R. A. Duine, “New perspectives for Rashba spin-orbit coupling,” *Nat. Mater.* **14**, 871 (2015).
- [74] M. Sato and Y. Ando, “Topological superconductors: a review,” *Rep. Prog. Phys.* **80**, 076501 (2017).
- [75] Ch.-K. Chiu, J. C. Y. Teo, A. P. Schnyder, and Shinsei Ryu, “Classification of topological quantum matter with symmetries,” *Rev. Mod. Phys.* **88**, 035005 (2016).
- [76] A. Altland and M. R. Zirnbauer, “Nonstandard symmetry classes in mesoscopic normal-superconducting hybrid structures,” *Phys. Rev. B* **55**, 1142 (1997).
- [77] S. Ryu, A. P. Schnyder, A. Furusaki, and A. W. W. Ludwig, “Topological insulators and superconductors: tenfold way and dimensional hierarchy,” *New J. Phys.* **12**, 065010 (2010).
- [78] S. Tewari and J. D. Sau, “Topological invariants for spin-orbit coupled superconductor nanowires,” *Phys. Rev. Lett.* **109**, 150408 (2012).
- [79] V. Gurarie, “Single-particle Green’s functions and interacting topological insulators,” *Phys. Rev. B* **83**, 085426 (2011).
- [80] A. Kobińska, N. Sedlmayr, M. M. Maška, and T. Domański, “Dimerization-induced topological superconductivity in a Rashba nanowire,” *Phys. Rev. B* **101**, 085402 (2020).
- [81] G. B. Lesovik and I. A. Sadovskyy, “Scattering matrix approach to the description of quantum electron transport,” *Phys.-Usp.* **54**, 1007–1059 (2011).
- [82] A. R. Akhmerov, J. P. Dahlhaus, F. Hassler, M. Wimmer, and C. W. J. Beenakker, “Quantized conductance at the Majorana phase transition in a disordered superconducting wire,” *Phys. Rev. Lett.* **106**, 057001 (2011).
- [83] C. W. J. Beenakker, J. P. Dahlhaus, M. Wimmer, and A. R. Akhmerov, “Random-matrix theory of Andreev reflection from a topological superconductor,” *Phys. Rev. B* **83**, 085413 (2011).
- [84] T. Ö. Rosdahl, A. Vuik, M. Kjaergaard, and A. R. Akhmerov, “Andreev rectifier: A nonlocal conductance signature of topological phase transitions,” *Phys. Rev. B* **97**, 045421 (2018).
- [85] I. C. Fulga, F. Hassler, A. R. Akhmerov, and C. W. J. Beenakker, “Scattering formula for the topological quantum number of a disordered multimode wire,” *Phys. Rev. B* **83**, 155429 (2011).
- [86] T.-P. Choy, J. M. Edge, A. R. Akhmerov, and C. W. J. Beenakker, “Majorana fermions emerging from magnetic nanoparticles on a superconductor without spin-orbit coupling,” *Phys. Rev. B* **84**, 195442 (2011).
- [87] P. Zhang and F. Nori, “Majorana bound states in a disordered quantum dot chain,” *New J. Phys.* **18**, 043033 (2016).
- [88] F. Domínguez, J. Cayao, P. San-Jose, R. Aguado, A. L. Yeyati, and E. Prada, “Zero-energy pinning from interactions in Majorana nanowires,” *npj Quantum Materials* **2**, 13 (2017).
- [89] J. Cayao, A. M. Black-Schaffer, E. Prada, and R. Aguado, “Andreev spectrum and supercurrents in nanowire-based SNS junctions containing majorana bound states,” *Beilstein J. Nanotechnol.* **9**, 1339–1357 (2018).
- [90] M. Z. Hasan and C. L. Kane, “Colloquium: Topological insulators,” *Rev. Mod. Phys.* **82**, 3045 (2010).
- [91] A. Bansil, H. Lin, and T. Das, “Colloquium: Topological band theory,” *Rev. Mod. Phys.* **88**, 021004 (2016).
- [92] M. S. Rider, S. J. Palmer, S. R. Pockock, X. Xiao, P. Arroyo Huidobro, and V. Giannini, “A perspective on topological nanophotonics: Current status and future challenges,” *J. Appl. Phys.* **125**, 120901 (2019).
- [93] P. Szumniak, D. Chevallier, D. Loss, and J. Klinovaja, “Spin and charge signatures of topological superconductivity in Rashba nanowires,” *Phys. Rev. B* **96**, 041401(R) (2017).
- [94] Ch. W. Groth, M. Wimmer, A. R. Akhmerov, and X. Waintal, “Kwant: a software package for quantum transport,” *New J. Phys.* **16**, 063065 (2014).
- [95] M. Wimmer, A. R. Akhmerov, J. P. Dahlhaus, and C. W. J. Beenakker, “Quantum point contact as a probe of a topological superconductor,” *New J. Phys.* **13**, 053016 (2011).
- [96] M. Kjaergaard, F. Nichele, H. J. Suominen, M. P. Nowak, M. Wimmer, A. R. Akhmerov, J. A. Folk, K. Flensberg, J. Shabani, C. J. Palmstrøm, and C. M. Marcus, “Quantized conductance doubling and hard gap in a two-dimensional semiconductor-superconductor heterostructure,” *Nat. Commun.* **7**, 12841 (2016).
- [97] H. Zhang, Ch.-X. Liu, S. Gazibegovic, D. Xu, J. A. Logan, G. Wang, N. van Loo, J. D. S. Bommer, M. W. A. de Moor, D. Car, R. L. M. Op het Veld, P. J. van Veldhoven, S. Koelling, M. A. Verheijen, M. Pendharkar, D. J. Pennachio, B. Shojaei, J. S. Lee, Ch. J. Palmstrøm, E. P. A. M. Bakkers, S. Das Sarma, and L. P. Kouwenhoven, “Quantized Majorana conductance,” *Nature* **556**, 74 (2018).
- [98] Hao Zhang, Dong E. Liu, Michael Wimmer, and Leo P. Kouwenhoven, “Next steps of quantum transport in majorana nanowire devices,” *Nat. Commun.* **10**, 5128 (2019).
- [99] J. Chen, P. Yu, J. Stenger, M. Hocevar, D. Car, S. R. Plissard, E. P. A. M. Bakkers, T. D. Stanescu, and S. M. Frolov, “Experimental phase diagram of zero-bias conductance peaks in superconductor/semiconductor nanowire devices,” *Sci. Adv.* **3**, e1701476 (2017).
- [100] S. Ikegaya, Y. Asano, and D. Manske, “Anomalous non-local conductance as a fingerprint of chiral Majorana edge states,” *Phys. Rev. Lett.* **123**, 207002 (2019).
- [101] S. Das Sarma, J. D. Sau, and T. D. Stanescu, “Splitting of the zero-bias conductance peak as smoking gun evidence for the existence of the Majorana mode in a superconductor-semiconductor nanowire,” *Phys. Rev. B* **86**, 220506(R) (2012).
- [102] Z. Cao, H. Zhang, H.-F. Lü, W.-X. He, H.-Z. Lu, and X. C. Xie, “Decays of Majorana or Andreev oscillations induced by steplike spin-orbit coupling,” *Phys. Rev. Lett.* **122**, 147701 (2019).